HHS Public Access

Author manuscript

Dev Cell. Author manuscript; available in PMC 2023 April 11.

Published in final edited form as:

Dev Cell. 2022 April 11; 57(7): 839–853.e6. doi:10.1016/j.devcel.2022.02.023.

Excess Neuropeptides in Lung Signal through Endothelial Cells to Impair Gas Exchange

Jinhao Xu[1,2], **Le Xu**[1], **Pengfei Sui**[3], **Jiyuan Chen**[4], **Esteban A. Moya**[5], **Patrick Hume**[6], **William J. Janssen**[6], **Jason M. Duran**[7], **Patricia Thistlethwaite**[8], **Aaron Carlin**[9], **Peter Gulleman**[10], **Brandon Banaschewski**[11], **Mary Kate Goldy**[11], **Jason X.-J. Yuan**[4], **Atul Malhotra**[4], **Gloria Pryhuber**[12], **Laura Crotty-Alexander**[4,13], **Gail Deutsch**[14], **Lisa R. Young**[10,11], **Xin Sun**[1,2,15,*]

[1]Department of Pediatrics, School of Medicine, University of California San Diego, La Jolla, CA 92093, USA

[2]Department of Biological Sciences, University of California San Diego, La Jolla, CA 92093, USA

[3]CAS Center for Excellence in Molecular Cell Science, Shanghai Institute of Biochemistry and Cell Biology, Chinese Academy of Sciences, 320 Yueyang Road, Shanghai 200031, China

[4]Division of Pulmonary, Critical Care and Sleep Medicine, School of Medicine, University of California San Diego, La Jolla, CA 92121, USA

[5]Division of Physiology, Department of Medicine, University of California San Diego, La Jolla, CA 92093, USA

[6]Department of Medicine, National Jewish Health, Denver, CO 80206, USA

[7]Division of Cardiology, Department of Internal Medicine, University of California San Diego Medical Center, La Jolla, CA 92037, USA

[8]Division of Cardiothoracic Surgery, University of California San Diego, La Jolla, CA 92093, USA

[9]Division of Infectious Diseases and Global Public Health, Department of Medicine, University of California San Diego, La Jolla, CA 92093, USA.

[10]Department of Pediatrics, Vanderbilt University Medical Center, Nashville, TN 37232, USA

[11]Division of Pulmonary and Sleep Medicine, Department of Pediatrics, Children's Hospital of Philadelphia, PA 16104, USA

[*]Correspondence to: xinsun@health.ucsd.edu.

AUTHOR CONTRIBUTIONS

J.X. X.S. and L.R.Y. conceived and designed experiments. J.X. and X.S. interpreted data. J.X., L.X., P.S., J.C., E.A.M., P.H., W.J.J., J.M.D., P.T., A.C., P.G., B.B., M.K.G., L.CA. and G.D. performed experiments and provided tissues. J.X. and L.X. analyzed single-cell RNA-seq data and generated figures. A.M., G.P., G.D., L.R.Y. and X.S. provided supervision and support. J.X. and X.S. wrote the manuscript with input from the other authors.

DECLARATION OF INTERESTS

X.S. is a member of the advisory board for Developmental Cell. J.X., L.R.Y. and X.S. have one related Patent Cooperation Treaty (PCT) application approved by World Intellectual Property Organization (WIPO) with number WO2020252368.

[12]School of Medicine and Dentistry, University of Rochester Medical Center, Rochester, NY 14642, USA

[13]Veterans Affairs San Diego Healthcare System, La Jolla, CA 92161, USA

[14]Department of Laboratories, Seattle Children's Hospital, University of Washington, Seattle, WA 98105, USA

[15]Lead Contact

SUMMARY

While increased neuropeptides are often detected in lungs that exhibit respiratory distress, whether they contribute to the condition is unknown. Here we show in a mouse model of neuroendocrine cell hyperplasia of infancy, a pediatric disease with increased pulmonary neuroendocrine cells (PNECs), excess PNEC-derived neuropeptides are responsible for pulmonary manifestations including hypoxemia. In mouse postnatal lung, prolonged signaling from elevated neuropeptides such as calcitonin gene-related peptide (CGRP) activate receptors enriched on endothelial cells, leading to reduced cellular junction gene expression, increased endothelium permeability, excess lung fluid, and hypoxemia. Excess fluid and hypoxemia were effectively attenuated by either prevention of PNEC formation, inactivation of CGRP gene, endothelium-specific inactivation of CGRP receptor gene, or treatment with CGRP receptor antagonist. Neuropeptides were increased in human lung diseases with excess fluid such as acute respiratory distress syndrome. Our findings suggest that restricting neuropeptide function may limit fluid and improve gas exchange in these conditions.

Blurb:

Xu et al. show that increased pulmonary neuroendocrine cells (PNECs) and secreted neuropeptides can cause poor gas exchange. In neuroendocrine hyperplasia of infancy (NEHI) mice, increased CGRP from PNECs causes vessel leakage, excess fluid and poor oxygenation. These findings suggest neuropeptides as therapeutic targets for conditions with excess lung fluid.

Graphical Abstract

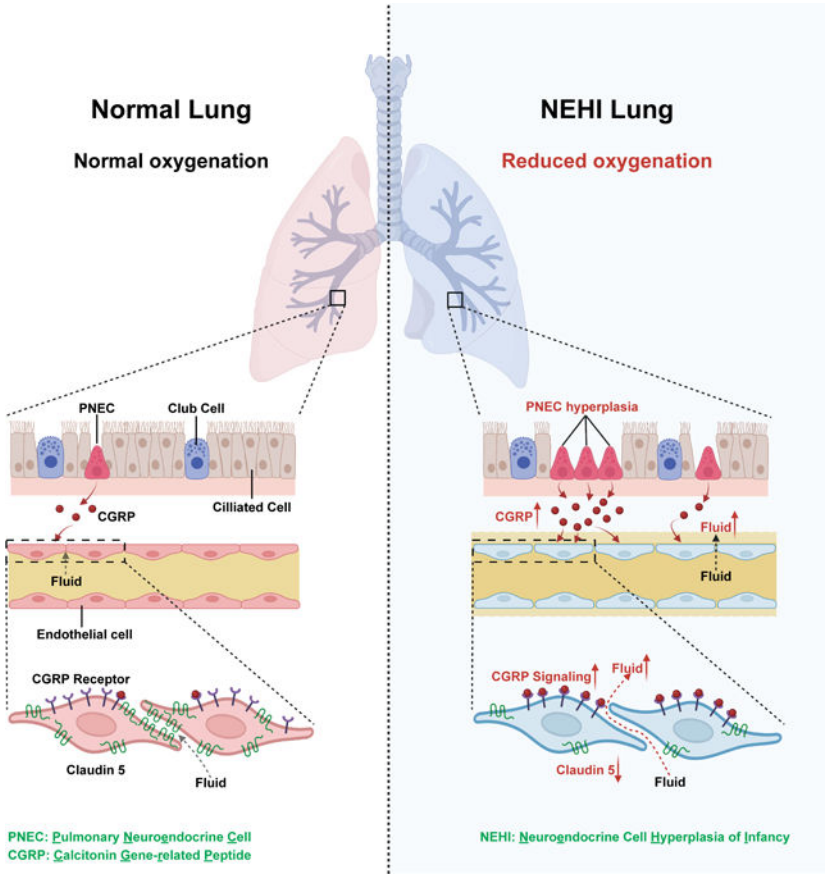

INTRODUCTION

Efficient gas exchange requires matched conductance of air and blood to the ~480 million alveoli in lung (Ochs et al., 2004), with diffusion of oxygen and carbon dioxide across the alveolar epithelial and endothelial barriers. Disruption of barriers, such as in acute respiratory distress syndrome (ARDS) caused by lung injury or infection, leads to excess fluid in the interstitial and/or the alveolar space, impeding gas exchange and causing respiratory distress. While multiple mechanisms contribute to ARDS, increases in select neuropeptides have been documented in the lungs of ARDS patients as well as in ARDS animal models (Espiritu et al., 1992). However, whether excess neuropeptides contribute to respiratory distress has not been addressed.

In the lung, a major cellular source of neuropeptides is pulmonary neuroendocrine cells (PNECs). PNECs represent a rare, and evolutionarily conserved airway epithelial cell population (Xu et al., 2020). *In vitro*, these specialized cells respond to stimuli such as nicotine, hypoxia and mechanical stretch by secreting potent bioactive neuropeptides and neurotransmitters (Cutz et al., 2007). *In vivo*, PNECs are activated following allergen challenge and are essential for amplifying allergen-induced asthmatic responses (Sui et al., 2018). Increased PNECs have been recognized in a variety of lung diseases, including bronchopulmonary dysplasia (BPD), asthma, pulmonary hypertension, sudden infant death

syndrome, and bronchiolitis obliterans (Cutz et al., 2007). However, it is debated whether the increase of this rare airway cell type is the cause or the consequence of poor gas exchange, and the repertoire and mechanisms governing PNEC function *in vivo* remains poorly understood.

Neuroendocrine cell hyperplasia of infancy (NEHI) is a rare childhood interstitial lung disease with unexplained and persistent respiratory symptoms (Deterding et al., 2005). NEHI patients are typically asymptomatic at birth but present with insidious onset of tachypnea, hypoxemia, crackles on chest auscultation, and failure to thrive in the first few months to years of age (Liptzin et al., 2020). A central puzzle with NEHI is the absence of alveolar simplification, a pathological feature that accompanies other conditions with gas exchange deficiency such as in chronic obstructive pulmonary disease (COPD) and bronchopulmonary dysplasia (BPD). In contrast to the lack of structural defect in the alveoli, the defining histological feature of NEHI is the characteristic PNEC hyperplasia as aggregates termed neuroendocrine epithelial bodies in the distal airways and alveolar ducts. However, it is debated whether the increase of a rare airway cell type would explain hypoxemia and respiratory symptoms. Most children with NEHI require supplemental oxygen for many years, as no disease-specific treatment for NEHI is currently available (Nevel et al., 2018).

In the present study, we established a mouse model of NEHI by generating mice that carry the first identified NEHI patient genetic variant, a point mutation in the transcription factor gene *NKX2–1* (Young et al., 2013). The mutant mice faithfully recapitulated key aspects of the clinical and pathologic phenotypes observed in children with NEHI. Through generation of multiple compound mutant, we demonstrated that increased PNECs and their associated neuropeptides are responsible for NEHI physiological phenotypes including reduced oxygenation. More importantly, mechanistic dissection revealed that excess PNEC production of neuropeptides such as calcitonin gene-related peptide (CGRP) signals through receptors on the endothelial cells to disrupt endothelial barrier, leading to excess fluid in lung. Treatment with a CGRP receptor antagonist reduced lung fluid and improved gas exchange in the NEHI model, raising the possibility that dampening excess neuropeptide signaling may help improve respiratory function.

RESULTS

Nkx2–1$^{R161L/R161L}$ Mutants Recapitulate Key Features of NEHI

To establish an animal model of NEHI, we used CRISPR/Cas9 technology to generate mice that carry an allele termed *Nkx2–1*^{R161L}, corresponding to the first patient mutation found in a family with NEHI (Figure 1A and 1B, Figure S1A) (Young et al., 2013). One round of CRISPR injection yielded 19 pups, 5 of which carried the intended change. To minimize effects of possible off-target mutation in any given founder, F1 progeny from different founders were bred to each other and phenotyping was carried out in their progeny.

To address if mice carrying the *Nkx2–1*^{R161L} allele recapitulated NEHI phenotypes, we started with assessment of PNEC hyperplasia, the namesake feature of NEHI. By counting CGRP+ cells in whole lung lobes and assaying for transcript level of PNEC markers *Ascl1*

and *Calca* (encoding CGRP), we found that *Nkx2–1*$^{R161L/R161L}$ mutants (hereafter referred to as *Nkx2–1*$^{L/L}$ mutants) exhibited increased numbers of PNECs compared to heterozygous (*Nkx2–1*$^{L/+}$) and wildtype (*Nkx2–1*$^{+/+}$) littermate controls (Figure 1C and 1D). A majority of the increased PNECs were found along the airway where PNECs are normally positioned (Figure 1E–1G). There was also a minor contribution (~6% of the total) from ectopic CGRP+ cells scattered in the alveolar region (Figure 1C, 1H–1J). In reviewing lung biopsies from NEHI patients, we found evidence of a variable number of ectopic PNECs in the alveolar region, in addition to the documented increases in the airway (Figure 1K). The findings in NEHI mouse model were supported by co-staining of another PNEC marker Synaptophysin (SYP) together with CGRP (Figure S1B–S1B"). Quantification revealed that the CGRP+ PNEC proportion remained unchanged in *Nkx2–1*$^{L/L}$ mutants compared to other controls, further confirming PNEC number increase (Figure S1C).

In contrast to PNEC hyperplasia, the number and distribution of ciliated cells and club cells appeared normal in *Nkx2–1*$^{L/L}$ mutants compared with controls (Figure S1D–S1F, S1D'-S1F'). There was no ectopic presence of basal cells in the intrapulmonary airway of mouse mutants, similar to controls. While goblet cells are present at baseline in normal human airways, their prominence has not been documented in NEHI. However, in contrast to the complete absence of goblet cells in mouse airway, in *Nkx2–1*$^{L/L}$ mutants, some distal airway cells co-expressed both the club cell marker SCGB1A1 and the goblet cell marker MUC5AC (Figure S1G–S1K). Furthermore, in *Nkx2–1*$^{L/L}$ mutants, the expression of key type 2 immunity cytokines such as *Il5* and *Il13* remained normal, suggesting that there is no heightened immune phenotype, consistent with the lack of inflammation in NEHI patient lungs (Figure S1L). Analogous to NEHI patient lungs, *Nkx2–1*$^{L/L}$ mouse mutant lungs exhibit normal lung size, normal alveolar architecture as quantified by mean linear intercept (MLI) and normal distribution of alveolar type 1 and type 2 (AT1 and AT2) cells by both immunostaining and qRT-PCR analysis (Figure S1M–S1X).

NEHI patients have normal birth weight but frequently exhibit failure to thrive by a few months of age, thought to be attributed to their chronic respiratory disease including tachypnea and hypoxemia. Similarly, *Nkx2–1*$^{L/L}$ mutants were had normal birth weight but displayed increasing growth retardation compared to littermate controls starting at P10 (Figure 1L and 1M). Importantly, *Nkx2–1*$^{L/L}$ mutants also exhibited low oxygen saturations as measured by SpO_2 (Figure 1N). Taken together, these observations indicate that the *Nkx2–1*$^{L/L}$ mouse mutants faithfully recapitulate key histological features and physiological symptoms observed in NEHI patients, providing a mouse model of this disease.

PNEC Hyperplasia was Associated with Increased Cell Specification rather than Proliferation

The mechanism underlying PNEC hyperplasia in NEHI has been debated, with consideration of increased cell specification versus increased proliferation of existing PNECs. To distinguish between these possibilities using the mouse model, we first determined the earliest time point when increased PNECs were detected by tracing the expression of *Ascl1*, a key PNEC cell fate marker. We found that *Ascl1* expression is already increased at embryonic day (E) 13.5, the stage when PNEC fate is normally specified

(Figure 2A) (Kuo and Krasnow, 2015). However, by EdU labeling at this timepoint, there was no change in epithelial proliferation in *Nkx2–1*$^{L/L}$ lungs compared to control genotypes (Figure 2B).

As *Ascl1* is also essential for PNEC specification (Ito et al., 2000), to directly test the possibility that PNEC hyperplasia in this NEHI model is due to increased specification, we generated *Nkx2–1*$^{L/L}$*; Ascl1*$^{-/-}$ double mutants. The double mutant mice died at birth, likely due to known requirement for *Ascl1* outside of the lung (Ito et al., 2000). When analyzed just before birth at E18.5, the double mutants showed a complete absence of PNECs, including those in the airway and alveolar regions (Figure 2C–2F). Consistent with the dependence of ectopic alveolar PNECs on *Ascl1*, lineage-tracing using *Ascl1*^{creER}*; R26R*$^{LSL\text{-}tdTomato}$*; Nkx2–1*$^{L/L}$ mice showed that the ectopic alveolar CGRP+ cells are derived from the *Ascl1* lineage (Figure S2A and S2B). Furthermore, these CGRP+ cells do not express HOPX or pro-SPC, markers for AT1 and AT2 cells, respectively, despite their localization in the alveolar region (Figure S2C and S2D). Collectively, these findings suggest that PNEC hyperplasia is due to increased *Ascl1*-dependent specification.

Nkx2–1$^{L/L}$ Mice Exhibited Increased Expression of *Sox2* and Decreased Expression of Notch Pathway Genes, Behaving as Partial Loss-of-function Mutants

After establishing that the increase of *Ascl1* is responsible for PNEC hyperplasia, we next dissected the molecular pathway from *Nkx2–1*^{L} mutation to *Ascl1* increase. Previous studies show that NKX2–1 represses the expression of *Sox2* (Domyan et al., 2011; Que et al., 2007). In turn, SOX2 inhibits the expression of *Notch*, and NOTCH activation induces the expression of *Hes1*, which inhibits the expression of *Ascl1* (Li et al., 2013; Xu et al., 2014). By qRT-PCR at E13.5, we observed an increase in *Sox2* and a decrease in Notch pathway genes including *Notch1*, *Notch2* and *Hes1* in *Nkx2–1*$^{L/L}$ lungs (Figure 2G). This increase in SOX2 persisted in postnatal stages as validated by anti-SOX2 antibody staining and qRT-PCR (Figure 2H–2K). Tracking back to normal embryonic lung, there is a clear correlation between higher SOX2 expression and PNEC cell fate (Figure S2E). These results are consistent with a genetic pathway from *Nkx2–1* to *Sox2*, to Notch signaling, resulting in regulation of *Ascl1* expression and PNEC specification (Figure 2L).

The direction of gene expression changes downstream of *Nkx2–1* suggests that *Nkx2–1*^{L} is a loss-of-function allele and inactivation of *Nkx2–1* would lead to increased PNECs. This notion is counter to the report that PNECs were absent in the *Nkx2–1*$^{-/-}$ null mutant, which also exhibited an early halt in overall lung development (Li et al., 2013). To resolve this discrepancy, we bypassed the early requirement for *Nkx2–1* in lung specification and inactivated the gene just prior to PNEC specification. In *Nkx2–1*$^{creER/F}$ conditional mutants, we observed a significant upregulation of PNEC markers by both immunostaining and qRT-PCR analysis (Figure S2F–S2H).

To further confirm that *Nkx2–1*^{L} is a loss-of-function allele, we performed a classical genetic complementation test by mating mice carrying the *Nkx2–1*^{L} allele to mice carrying the *Nkx2–1*$^{-}$ null allele. PNEC increase was detected in *Nkx2–1*$^{L/-}$ mutants compared to controls while the lung size remained largely normal (Figure S2I–S2K). Unlike in *Nkx2–1* null mutants where trachea and esophagus failed to separate (Minoo et al., 1999), they

separated normally in *Nkx2–1*$^{L/-}$ mutants. These results together suggest that *Nkx2–1*^{L} acts as a partial loss-of-function allele.

Nkx2–1$^{L/L}$ Mutants Developed Excess Fluid in Lung

A key puzzle in NEHI is the cause of hypoxemia given that lung size and alveolar architecture appears normal. Establishment of the animal model allowed us to investigate a range of parameters using invasive approaches in mutants compared to littermate controls. Since *Nkx2–1*$^{L/L}$ mutants showed improved body weight and oxygenation with age, similar as what has been reported in NEHI patients (Figure S3A–S3F) (Deterding et al., 2005; Nevel et al., 2018). Therefore, we focused on early time points to evaluate potential pathophysiologic mechanisms. We found that the wet-to-dry (W/D) ratio of mutant lungs was statistically significantly increased at weaning (P22) and at the end of alveologenesis (P39) (Figure 3A and 3B). These data indicate that the overall excess fluid in lung is a quantifiable phenotype associated with the NEHI mouse model.

Preventing PNEC Formation Alleviated Excess Fluid, Reduced Oxygenation and Growth Defect in the NEHI Mouse Model

It has been long debated whether PNEC hyperplasia are causal for NEHI symptoms, are bystanders, or a consequence of the disease. To test these possibilities using the NEHI model, we genetically prevented the formation of PNECs in NEHI lung by generating *Nkx2–1*$^{L/L}$; *Shh*$^{cre/+}$; *Ascl1*$^{F/F}$ (hereafter referred to as *Nkx2–1*$^{L/L}$; *Ascl1*^{cKO} mutant). As in *Nkx2–1*$^{L/L}$*; Ascl1*$^{-/-}$ mutant, inactivation of *Ascl1* led to a complete absence of PNECs in *Nkx2–1*$^{L/L}$; *Ascl1*^{cKO} mutant (Figure S3G–S3I). But unlike the *Ascl*$^{-/-}$ mutant which died at birth due to global loss of *Ascl1*, the tissue-specific *Shh*$^{cre/+}$*; Ascl1*$^{F/F}$ mutant, and thereby the *Nkx2–1*$^{L/L}$; *Ascl1*^{cKO} mutant survived (Sui et al., 2018). We found that compound *Nkx2–1*$^{L/L}$; *Ascl1*^{cKO} mutants displayed improved body weight, normal lung W/D ratio and oxygen saturation level at P22 compared to either *Nkx2–1*$^{L/L}$ or *Ascl1*^{cKO} single mutants (Figure 3C–3F). These findings demonstrate that rather than being the consequence of NEHI, PNECs are key contributors to excess fluid, hypoxemia and growth retardation in the NEHI mouse model.

Genetic Inactivation of PNEC Products Alleviated Excess Fluid, Reduced Oxygenation and Growth Defect in the NEHI Mouse Model

Next, we investigated the molecular mediators that link PNEC hyperplasia to NEHI-like phenotypes. As PNECs are known for their production of highly bioactive neuropeptides and neurotransmitters, we focused on these products. CGRP, a key neuropeptide secreted by PNECs, can induce edema when injected in the paw (Brain et al., 1985; Newbold and Brain, 1993). To address if CGRP plays a role in the *Nkx2–1*$^{L/L}$ physiological phenotypes, we measured CGRP levels in bronchioalveolar lavage (BAL) fluid and found significant increases in CGRP levels in in *Nkx2–1*$^{L/L}$ mutants compared to controls, suggesting that upregulated *Calca* (encoding CGRP) gene expression resulted in elevated secreted protein (Figure 4A). In addition, intranasal administration of CGRP in early postnatal pups led to increased W/D ratio (Figure 4B and 4C), indicating that excess CGRP is sufficient to cause excess fluid in lung.

To test if increased CGRP may contribute to NEHI phenotypes, we inactivated CGRP gene in NEHI mutants by generating *Nkx2–1*$^{L/L}$*; Calc*$^{-/-}$ double mutants. As expected, in these double mutants, PNEC hyperplasia was still observed, while CGRP was at background level by staining and in BAL fluid (Figure 4D, Figure S4A–S4F). At P22, the *Nkx2–1*$^{L/L}$*; Calca*$^{-/-}$ double mutants displayed normal body weight, decreased lung W/D ratio and normal oxygen saturation compared to those of single mutants and *Nkx2–1*$^{L/+}$ controls (Figure 4E–4H). We note that the W/D ratio did not fully revert back to control level, suggesting that other PNEC products may contribute to the excess fluid phenotype. In support of this, inactivation of *Tac1*, which encodes substance P, another edema-inducing neuropeptide (Newbold and Brain, 1993), also led to partial reversal of the excess fluid phenotype in the *Nkx2–1*$^{L/L}$ mutant background (Figure S4G–S4I). These results indicate that PNEC products contribute significantly to excess fluid, reduced oxygen saturation and poor weight gain in mice.

Our previous study showed that PNECs are important for amplifying asthmatic response including goblet cell metaplasia following exposure to allergen (Sui et al., 2018). Thus, we also addressed if PNECs are responsible for the goblet cell metaplasia phenotype in *Nkx2–1*$^{L/L}$ mutants. We confirmed this possibility by the finding that few goblet cells were detected in *Nkx2–1*$^{L/L}$; *Ascl1*^{cKO} mutants (Figure S4J–S4M). We and others have shown that PNECs produce γ-aminobutyric acid (GABA), and GABA is required for allergen-induced goblet cell metaplasia phenotype (Barrios et al., 2019; Barrios et al., 2017; Sui et al., 2018; Xiang et al., 2007). To address if GABA is responsible for goblet cell metaplasia phenotype in the *Nkx2–1*$^{L/L}$ mutants, we inactivated vesicular GABA transporter gene *Vgat* which is required for GABA secretion, in the *Nkx2–1*$^{L/L}$ mutant background (*Nkx2–1*$^{L/L}$; *Shh*$^{cre/+}$; *Vgat*$^{F/F}$, hereafter referred to as *Nkx2–1*$^{L/L}$; *Vgat*^{cKO} mutant). Few goblet cells were detected in *Nkx2–1*$^{L/L}$; *Vgat*^{cKO} (Figure S4N and S4O). In contrast, goblet cell metaplasia persisted in *Nkx2–1*$^{L/L}$*; Calca*$^{-/-}$ mutants (Figure S4P and S4Q). Furthermore, pharmaceutical inhibition of $GABA_A$ receptor by antagonist Bicuculline also alleviated the phenotype (Figure S4R–S4W). Taken together, our data indicate that GABA produced by PNECs is a significant contributor to goblet cell metaplasia in the *Nkx2–1*$^{L/L}$ mutant.

Increased CGRP Acts through Receptors on Endothelial Cells to Downregulate Junction Protein Expression, Leading to Disruption of Barrier, Excess Fluid and Reduced Oxygenation

Next, we investigated how increased PNECs and their products could contribute to excess fluid in lung. It is known that CGRP binding to receptors functions through activating cAMP signaling (Aiyar et al., 1996). Consistent with increased signaling, in the *Nkx2–1*$^{L/L}$ mutant, whole lung qRT-PCR analysis showed upregulation of *Atf2* (also called *Creb2*) and *Creb3*, two effectors of cAMP signaling, while *Creb1* level was not significantly different from control (Figure 5A). To address how CGRP may contribute to excess fluid, we focused on endothelial cells because available single cell RNA-seq (scRNA-seq) data indicate that in both mouse and human lungs, the expression of obligatory CGRP receptor gene *Calcitonin receptor-like* (*Calcrl*, or *Crlr*) is highly enriched in all subpopulations of endothelial cells (Figure S5A–D) (Du et al., 2017; Travaglini et al., 2020; Wang et al.,

2020). We generated scRNA-seq data using both Mut (*Nkx2–1*$^{L/L}$) and Ctrl (*Nkx2–1*$^{+/+}$) lungs at P22, which captured all major endothelial cell types (Figure 5B and 5C). Cell-cell communication analysis revealed a clear PNEC-endothelial signaling signature highlighted by CGRP-CALCRL pairing (Figure S5E–G). Among the top differentially expressed genes is *Rras*, a key cAMP-regulated downstream effector gene. In the *Nkx2–1*$^{L/L}$ mutant lung, *Rras* is downregulated in multiple endothelial cell populations, including vein and both capillary populations (Figure 5D). This is consistent with data from endothelium cell culture showing that prolonged activation of CREB signaling reduces *Rras* level (Perrot et al., 2018).

Results from endothelium culture experiments also showed that prolonged cAMP activation, functioning through repressing *Rras*, disrupts adherence junction VE-Cadherin (also called CDH5) function, leading to increased endothelium permeability (Perrot et al., 2018). Previous studies also showed that CDH5 can regulate endothelium-specific tight junction factors such as *Cldn5* with a critical role in endothelium barrier maintenance in lung (Jang et al., 2011; Taddei et al., 2008). These findings led us to assess junctional proteins and endothelium permeability in the *Nkx2–1*$^{L/L}$ mutant lung. We found that compared to control, the mutant lungs showed quantitatively reduced CDH5 protein by western blot analysis (Figure 5E and 5F), reduced *Cldn5* gene expression by qRT-PCR, and reduced CLDN5 protein by western blot analysis as well as by immunostaining (Figure 5G–5K). Interestingly, immunostaining also showed that such CLDN5 downregulation was no longer apparent in endothelial cells of the *Nkx2–1*$^{L/L}$; *Ascl1*^{cKO} or *Nkx2–1*$^{L/L}$; *Calca*$^{-/-}$ compound mutants where wet-dry ratio and other physiological abnormalities were attenuated (Figure 5L and 5M). To assess barrier integrity, we introduced Evans Blue dye into the blood stream and assayed for dye retention in lung following an established barrier assay protocol (Smith et al., 2019). The mutant lungs showed increased dye retention compared to control lungs, indicative of disrupted barrier and increased leakage (Figure 5O).

CGRP is a known vessel dilator and may contribute to excess fluid by allowing more fluid in vessels (Brain and Grant, 2004). To address if vessel engorgement may be a reason for excess fluid in the NEHI mutant lung, we performed angiogram assay by injecting dye into the vessels. We found that vessel size and number remained largely normal in the mutant compared to control (Figure S5H–S5J). Interestingly, in a subset of the lobes in the mutants (n=3/4 animals) but not in controls (n=0/3 animals), we also detected regional leakage in the distal vessels shortly after dye injection, consistent with results from Evans Blue assay (Figure 5P and 5Q). These findings together raised the possibility that a breach of barrier may contribute to excess fluid in the *Nkx2–1*$^{L/L}$ mutant.

To test directly if excess CGRP signaling on endothelial cells could contribute to NEHI phenotypes *in vivo*, we inactivated *Crlr* specifically in endothelial cells by generating *Nkx2–1*$^{L/L}$; *Cdh5-cre; Crlr*$^{F/F}$ compound mutants (hereafter referred to as *Nkx2–1*$^{L/L}$; *Crlr*^{cKO} mutant). *Nkx2–1*$^{L/L}$; *Crlr*^{cKO} mutants exhibited normal lung W/D ratio and oxygen saturation, demonstrating that signaling via CRLR receptor on endothelial cells contributed significantly to NEHI physiological phenotypes in *Nkx2–1*$^{L/L}$ mutants (Figure 5R and 5S).

To test if similar barrier disruption occurs in NEHI patients, we performed immunofluorescence staining on normal and NEHI lung biopsies. Expected increase of PNECs was captured by staining for specification marker PROX1 in NEHI biopsies compared to the control (Figure S5K and S5L). While not reaching statistical significance likely due to variability in human genetic background, age, fixation conditions used at the time of procurement and lengths of storage, there was a trend towards decrease of CLDN5/CD31 intensity ratio in NEHI biopsies compared to controls (Figure 5T–5V, Figure S5M–S5P), suggesting a potential downregulation of tight junction proteins in human NEHI lungs. Taken together with data from our NEHI mouse model, our findings support a role of excess CGRP in downregulating junctional proteins, compromising pulmonary endothelial barrier, leading to reduced oxygenation (Figure 5W).

Pharmacological Inhibition of CGRP Signaling Alleviated Excess Fluid, Reduced Oxygenation and Growth Defect in the NEHI Mouse Model

Findings from gene expression and genetic compound mutants suggest that repressing CGRP may be effective at attenuating abnormalities observed in the NEHI mouse model. To test this concept directly, we inhibited CGRP function locally by intranasal administration of BIBN-4096, a CGRP receptor antagonist at the postnatal stage (Figure 6A). Compared to vehicle DMSO treatment, BIBN-4096 treatment in the control genotype groups did not lead to detectable effects. In comparison, in *Nkx2–1*$^{L/L}$ mutants, BIBN-4096 treatment led to a clear attenuation of all key NEHI physiological phenotypes, including excess lung fluid, reduced oxygen saturation, and poor weight gain (Figure 6B–6D). By performing qPCR analyses, we found that the attenuation of physiological phenotypes was linked to reversal of molecular changes, including a downregulation of cAMP signaling as marked by *Atf2* expression level upon BIBN-4096 treatment (Figure S6A–S6D). Additionally, qPCR, western blot and immunostaining showed a reversal of CLDN5 RNA and protein levels and a trending reversal of CDH5 protein level in BIBN-4096-treated *Nkx2–1*$^{L/L}$ mutants compared to DMSO-treated vesicle control group (Figure 6E–6J). These results demonstrate the efficacy of CGRP receptor antagonist in treating NEHI symptoms in this animal model.

To address if increase of PNEC products such as CGRP may be relevant in other disease conditions with excess lung fluid, we investigated signaling changes in coronavirus disease 2019 (COVID-19) associated ARDS lungs, which feature excess fluid as the primary cause of death (Ackermann et al., 2020; Fox et al., 2020). We found that in lungs from patients who have succumbed to COVID-19, a majority of PNECs, as identified by their expression of GRP (also known as Bombesin), expressed CGRP (81.35% ± 4.686%, n=7 donors, Table S2 for donor metadata). There is a statistically significant increase ($p<0.0001$ and $p=0.0012$, respectively) over the proportion of PNECs expressing CGRP in non-ARDS controls from either surgical samples (19.34% ± 7.259%, n=4 donors) or autopsy samples (39.03% ± 8.135%, n=4 donors) (Figure 7A–7F). Furthermore, we also detected high CGRP+ PNECs (74.93% ± 1.668%, n=3 donors) in non-COVID ARDS samples (Figure 7G–7I). Consistent with the link between CGRP increase and CLDN5 downregulation in both *Nkx2–1*$^{L/L}$ mutants and NEHI biopsies (Figure 5), a significant decrease of CLDN5+ endothelial cells were also detected in ARDS samples (53.88% ± 24.67%, n=3 donors) compared to surgical (91.30% ± 5.908%, n=3 donors) or autopsy 88.02% ± 6.656%, n=4 donors) samples (Figure

7J–7P). A significant downregulation of CLDN5 was also reported in COVID-19 lung samples (D'Agnillo et al., 2021). While excessive lung damage and inflammation are likely the primary cause of profound damage in COVID and non-COVID ARDS, the staining data combined with our functional findings from the NEHI mouse model raised the possibility that increased PNEC production of neuropeptides may be an additional contributor to excess lung fluid in these conditions.

DISCUSSION

In this study, we present evidence from *in vivo* experiments demonstrating a fundamental mechanism of neuropeptidergic control of pulmonary vascular integrity and in turn, oxygenation. Increased PNECs and their secreted neuropeptides are necessary and sufficient to cause excess fluid in lung and compromised oxygenation. Given the absence of alveolar structural disruption and overt immune infiltration, the *Nkx2–1* mutant NEHI mouse model provides a streamlined experimental platform to evaluate the specific effects of PNEC-derived neuropeptides on lung function. The discovered mechanism is supported by several modes of robust *in vivo* rescues of NEHI phenotypes, including prevention of PNEC formation, inactivation of CGRP, endothelium-specific inactivation of CGRP receptor, and treatment with CGRP receptor antagonist.

Starting with a *NKX2–1* variant reported in a multigeneration familial cohort with NEHI, this mouse model of the disease has revealed step-by-step links from the candidate NEHI gene to cellular, molecular, and physiological phenotypes (Figure 2L, 5W and 7Q). The finding that disrupting PNEC formation in the *Nkx2–1* mutant background reversed NEHI-phenotypes addresses a long-standing debate and demonstrates that PNEC hyperplasia is a driver of symptoms.

We demonstrated that this particular *Nkx2–1* associated with NEHI is a partial loss-of-function allele. Reduced *Nkx2–1* function led to increased *Sox2* expression, decreased Notch signaling and increased *Ascl1* expression (Figure 2L). Results from the $Nkx2\text{–}1^{L/L};Ascl^{-/-}$ double mutant show that increased *Ascl1* is responsible for increased PNECs. Data from scRNA-seq, qRT-PCR, western blot analysis and antibody staining demonstrate that with increased PNECs, excess PNEC products such as CGRP signal to endothelial cells, resulting in prolonged activation of GPCR and downstream cAMP signaling, which lead to downregulation of Rras and junctional proteins essential for barrier maintenance (Figure 5W). A disruption of barrier is supported by increased Evans Blue dye retention and increased angiogram dye leakage. Across the various compound mutants, the tight association of changes in wet/dry ratio, reduced oxygen saturations and growth retardation parameters suggest that these phenotypes are likely linked (Figure 7Q). It remains possible that other mechanisms that may contribute to these NEHI phenotypes. Regardless of the relationship among poor gas exchange, excess lung fluid and decreased growth rate, the findings that disruption of neuropeptide signaling can reverse these defects demonstrates a significant role of neuropeptides in normal lung physiology.

Results in the present study uncovered a critical *in vivo* role of PNECs in regulating lung fluid. We note that the wet/dry ratio increase in the NEHI mouse model is mild in

comparison with that in animal models of ARDS (Gotts et al., 2019). We postulate that in NEHI, it is possible that vessel leakage and fluid accumulation is concentrated at small bronchiole/alveolar entrance areas near common sites of PNEC hyperplasia. This could explain how a limited increase in fluid volume could block gas exchange in a relatively large alveolar areas distal to blockage points, effectively reducing oxygenation. This possibility is consistent with the dye leakage pattern near distal vessels in the angiograms of NEHI mouse model. Local airway obstruction by fluid could also contribute to unexplained clinical findings in NEHI patients, including crackles on chest auscultation, as well as chest imaging which demonstrates hyperinflation and distinctive ground-glass opacities without architectural distortion (Young et al., 2011). Further studies are needed to understand how these murine model alterations in barrier and vascular integrity relate to findings in the human disease, though it is intriguing to consider the possibility that fluid homeostasis could be relevant.

We found that in the lungs of patients who succumbed to COVID-19 or non-COVID-19 ARDS, there was increased proportion of PNECs expressing CGRP. Increased substance P was also found in the pulmonary edema fluids of ARDS patients as well as a sheep model of ARDS (Espiritu et al., 1992). Our result that substance P-encoding *Tac1* null mutation can rescue NEHI phenotypes suggest that substance P may also play a notable role in inducing excess lung fluid. There are many known causes of ARDS, including infection induced damage and inflammation (Huppert et al., 2019; Matthay et al., 2019). Our findings here raise the possibility that neuropeptide-induced barrier disruption may serve as another molecular contributor. Forms of CGRP or CGRP receptor antagonists have been approved by FDA for the treatment of migraine, paving the way for considering them as a candidate treatment for conditions with excess fluid in lung (Olesen et al., 2004). In light of the knowledge that CGRP has vessel dilator activity, the potential effect of CGRP antagonism in exacerbating vessel constriction was addressed in their safe use in the treatment for migraine (Breen et al., 2021; MaassenVanDenBrink et al., 2016), and should also be carefully considered in their potential use for treating other diseases associated with excess neuropeptides.

Our study reaffirms the notion that investigating rare diseases can lead to discoveries of fundamental biological mechanisms. From NEHI, we uncovered that neuropeptides regulate lung fluid level, and in turn gas exchange efficiency. Aside from PNECs, neuropeptides such as CGRP and substance P can also be produced by nerves in the lung (Baral et al., 2018; Hennessy et al., 2017; Su et al., 2022). Outside of the lung, neuroendocrine cells and nerves are present in many peripheral tissues such as the intestine, stomach, prostate, etc. (Kaelberer et al., 2018; Xu et al., 2020). Future studies are needed to address if excess neuropeptide signaling may be a recurrent contributor to disease conditions with excess tissue fluid.

Limitations of the study

Although our NEHI mouse model captured key characteristics of the disease, there are remaining human patient features (e.g., crackles on chest auscultation) that cannot be reliably detected and rigorously investigated in mice. Overall, documented physiological

differences between human and mouse should be taken into consideration when interpreting physiological data from mice. Lastly, limited access to human samples (including NEHI and ARDS lung biopsies) has restrained our ability to quantitatively determine the link between increased neuropeptides and impaired endothelial barrier. This link could be further interrogated by obtaining and assaying tissues from additional donors.

STAR METHODS

RESOURCE AVAILABILITY

Lead Contact—Further information and requests for resources and reagents should be directed to and will be fulfilled by the lead contact, Dr. Xin Sun (xinsun@health.ucsd.edu).

Materials availability—Mice carrying the *Nkx2–1*^{R161L} allele will be made available upon request following standard signing of Materials Transfer Agreement in accordance with NIH Principles and Guidelines.

Data and code availability

- All raw sequencing data and processed files have been deposited in GEO under the series reference GEO: GSE171907 and are publicly available upon publication. Accession numbers are listed in the key resources table. Original western blot images have been deposited at Mendeley and are publicly available upon publication. The DOI is listed in the key resources table. Microscopy data reported in this paper will be shared by the lead contact upon request.
- This study does not report original code. All codes and algorithms used for single-cell RNA-seq analyses are listed in the key resources table.
- Any additional information required to reanalyze the data reported in this paper is available from the lead contact upon request.

EXPERIMENTAL MODEL AND SUBJECT DETAILS

Mice—All mice were housed in American Association for Accreditation of Laboratory Animal Care (AAALAC) accredited facilities and labs at University of California, San Diego. All animal husbandry and experiments were conducted under approved Institutional Animal Care and Use Committee (IACUC) guidelines. *Nkx2–1*^{R161L} mouse line was designed and generated in the Sun's lab, with the service of the University of Wisconsin-Madison Transgenic Core. *Ascl1*^{creERT2}, *Cdh5-cre*, *Nkx2–1*^{creERT2}, *Tac1*$^{-}$, *Vgat*^{fl}, and Ai14 (*R26R*$^{LSL\text{-}tdTomato}$) mice were purchased from JAX. *Calca*$^{-}$ was obtained from MMRRC-UNC. *Ascl1*^{fl} was a kind gift from Dr. Guoli Dai with permission from Dr. Francois Guillemot. *Crlr*^{fl} was a kind gift from Dr. Kathleen Caron. *Nkx2–1*^{fl} was a kind gift from Dr. Shioko Kimura. *Shh*^{cre} was a kind gift from Dr. Cliff Tabin. All mice were either bred in B6 background or have been back crossed to B6 background for at least 3 generations. Littermates were used as controls to minimize potential genetic background effects. Data from male and female mice were pooled into one group for analysis unless otherwise noted.

Human donors and tissue collection—Biopsies from 4 patients with the clinical and pathologic diagnosis of neuroendocrine cell hyperplasia of infancy and 4 age-matched control lungs (biopsied for other lung processes or from lobectomies with histologically normal lung adjacent to focal lesions; see Table S1 for metadata) were identified from a pathology database under a protocol approved by Seattle Children's Hospital Institutional Review Board.

Adult donor lung samples were procured under institutional approved protocols from the federal United Network of Organ Sharing via National Disease Research Interchange (NDRI) and International Institute for Advancement of Medicine (IIAM), at University of Rochester, University of California San Diego, or University of Colorado. Lungs were obtained from deceased donors who were either free of lung disease (n=4, non-ARDS autopsy controls), or succumbed to complications related to severe ARDS prior to COVID-19 pandemic (n=3, non-COVID-ARDS), or severe ARDS as a result of COVID-19 (n=7, COVID-ARDS). Lobectomy tissues without pathological lesion were collected as additional controls (n=4, non-ARDS lobectomy controls). Immunostaining was performed on fixed paraffin embedded lung samples. All tissues were obtained following fulfilment of institutionally approved informed consent protocol in each case.

METHOD DETAILS

Histology preparation, periodic acid–Schiff (PAS) staining and Mean Linear Intercept (MLI) quantification—Mice were euthanized under approved Institutional Animal Care and Use Committee (IACUC) guidelines. Lungs were inflated with 4% PFA at 35cm H_2O airway pressure, fixed overnight and then prepared for paraffin (6μm) or cryo (10~15 μm) sections. Goblet cells were stained using a periodic acid–Schiff (PAS) staining kit (Sigma). To quantify mean linear intercept (MLI), 10X H&E images were used. For each group, 3 mice per genotype, 3 sections per mouse and 3 independent fields per section were analyzed. Samples were compared using Student's t-test, by MLI ± S.D. with statistical significance called at $p<0.05$.

Immunofluorescent staining—The following primary antibodies were used at the indicated final concentration for immunofluorescence staining: rabbit anti-Synaptophysin polyclonal antibody [5 mg/ml] (Fisher), rabbit anti-Calcitonin gene-related peptide (CGRP) polyclonal antibody [2 mg/ml] (Sigma), rabbit anti-SCGB1A1 polyclonal antibody [5 mg/ml] (Seven Hills Bioreagents), rabbit anti-SPC polyclonal antibody [5 mg/ml] (SevenHills Bioreagents), mouse anti-MUC5AC monoclonal antibody [5 mg/ml] (MRQ-19, Sigma), syrian hamster anti-T1alpha (PDPN) polyclonal antibody [5 mg/ml] (Developmental Studies Hybridoma Bank), mouse anti-CLDN5 monoclonal antibody [5 mg/ml] (4C3C2, Invitrogen), rat anti-EMCN monoclonal antibody [10 mg/ml] (V.5C7, Santa Cruz), mouse anti-CGRP (human) monoclonal antibody [2 mg/ml] (Lifespan Biosciences) and rabbit anti-GRP polyclonal antibody [5 mg/ml] (Immunostar). The following secondary antibodies were used with the indicated final concentration: Cy3-conjugated goat anti-mouse IgG [2 mg/ml], Cy3-conjugated goat anti-rabbit IgG [2 mg/ml], FITC-conjugated goat anti-rabbit IgG [2 mg/ml], AF488-conjugated goat anti-rat IgG [2 mg/ml]. All images were acquired on ZEISS AxioImager 2. To quantify cells labeled by specific markers, 20X IF

images were used. For each group, at least 3 mice per genotype and at least 3 sections per mouse were analyzed. Sections were selected such that they were best matching each other and covering a range of different depths.

Immunofluorescent staining and quantification on control and NEHI lung biopsies—Immunostaining was carried out on formalin-fixed, paraffin-embedded 5-μm sections. The following antibodies were used: rabbit anti-CLDN5 monoclonal antibody (1:400; JM11–22, Invitrogen), mouse anti-CD31 monoclonal antibody (1:200; M0823, clone JC70A, Dako), rabbit anti-bombesin polyclonal antibody (1:500; ImmunoStar), and goat anti-PROX1 polyclonal antibody (1:200; R&D Systems).

For immunofluorescence staining antibodies were incubated overnight at room temperature and pretreated with citrate pH 6.0 antigen retrieval followed by endogenous biotin block. The following secondary antibodies were used: FITC and Cy3-conjugated donkey anti-rabbit IgG, FITC and Cy3-conjugated donkey anti-mouse IgG and FITC (all 1:500 from Jackson Immunoresearch). PROX1 was developed with biotinylated anti-goat antibody, streptavidin-biotin-peroxidase complex (both Vector Laboratories) and visualized with FITC TSA signal amplification system (PerkinElmer). Coverslips were mounted using Vectashield fluorescent mounting medium with DAPI (Vector Laboratories).

All slides were stained, imaged, and quantified together. For each subject, immunostaining for CLDN5 and CD31 was quantified in up to 5 random sections using the same magnification (20x), exposure time, lamp intensity and camera gain. No image processing was carried out prior to intensity analysis. CLDN5 immunostained area was expressed as a percentage of CD31 immunostained area. Images were visualized and captured with a digital camera mounted on a Nikon Eclipse 80i microscope using NIS-Elements Advanced Research Software v4.13 (Nikon Instruments Inc., Melville, NY).

EdU analysis for cell proliferation—For EdU analysis of cell proliferation, 1 ml of 400 mM EdU solution (Thermo Scientific) was intraperitoneally injected into pregnant females. Mice were sacrificed 1 hour after EdU injection. Embryonic lungs were fixed in 4% PFA overnight and prepared for cryo-sectioning (10 mm). EdU was detected using the Click-iT EdU Kit with Alexa Fluor 488 (Invitrogen).

Oxygen Saturation (SpO_2) measurement—Pups were shaved and anesthetized by isoflurane while measurements were conducted using pulse-ox (MouseOxPlus, Starr Life Sciences). SpO_2 reads were recorded after 5 minutes of stable reading. Note that investigators were not, and cannot be, blinded to experimental groups during this measurement as the growth retardation of some mutant individuals was evident at this stage.

Lung Wet-to-Dry ratio measurement—Individual lungs were harvested immediately after euthanasia. Excessive blood was wiped off by Kimwipe and wet weight $\mathbf{m_w}$ was measured. Lungs were then placed on foil at 70°C for 24 hours. Dry weight $\mathbf{m_d}$ was measured. Wet-to-dry ratio was calculated as: $\mathbf{W/D\ ratio = m_w/m_d}$.

Bronchoalveolar Lavage (BAL)—After sacrifice, each mouse was intratracheally injected with 1 ml saline using 1ml insulin syringe (Medline Industries). Approximately 800ul BAL was then recovered. The BAL was analyzed for for protein concentration by Pierce™ BCA Protein Assay kit (Thermo Scientific), cell counts by hemocytometer, or neuropeptide level using ELISA.

ELISA—BAL CGRP concentration was measured by CGRP (rat) EIA Kit (Cayman Chemicals). A volume of 100μ BAL was used in each well. Final readout was performed by microplate reader (TECAN). The concentration presented is adjusted with the background detection set as 0.

Tissue dissociation and sorting of single cells—After euthanasia and before tissue harvest, mice were transcardially perfused with 12 ml of cold DPBS (Life Technology). Whole lungs were mechanically dissociated in GentleMACS C tubes (Miltenyi Biotec) by running mouse lung 1–2 program on GentleMACS (Miltenyi Biotec). Lung pieces were then digested by shaking (~150 rpm) in 5 ml of PRMI 1640 (Thermo Scientific) with 10% FBS, 1mM HEPES (Life Technology), 1mM $MgCl_2$ (Life Technology), 1mM $CaCl_2$ (Sigma-Aldrich), 0.525mg/ml collagenase/dispase (Roche) and 0.25 mg DNase I (Roche) for 30 min at 37°C, followed by straining through a 70-mm filter. Red blood cells were removed by adding 1mL RBC lysis buffer (Biolegend) to each tube and incubate at room temperature for 1min.

The single-cell suspensions from above were then pelleted (1500 rpm, 4°C, 5 min), counted with hemocytometer and diluted to ~1×10^6 cells per ml. They were stained with Fc blocking antibody (5 mg/ml, BD) and live/dead dye (1:2000, Ghost Dye Red 780, TONBO biosciences) at 4°C for 30 min. The cells were washed with DPBS and then incubated with surface marker antibody cocktail for 30 min at 4°C. For sorting endothelial and epithelial cells, the following antibodies were used (all antibodies were from Biolegend): 1:500 APC-conjugated anti-CD326 (G8.8); 1:500 BV510-conjugated anti-CD45 (30-F11); 1:500 PE-conjugated anti-CD31 (MEC13.3). Cell sorting was performed on a FACSAriaII high speed sorter (BD Biosciences) with four lasers (405 nm, 488 nm, 561 nm, and 640 nm). All data were further analyzed and plotted with FlowJo software (Treestar).

Droplet-based high throughput Single-Cell RNA-seq and data analysis—After FACS, sorted cells were counted and processed using Chromium Single Cell 3’ v3 kit (10X Genomics). Sequencing was carried out on NovaSeq (Illumina) platform at the Institute for Genomic Medicine, UCSD. Cell Ranger package (version 3.0.2) was used to align the raw reads onto the mouse reference genome (GRCm38) and generate the feature-barcode matrix. Next, R package Seurat (version 4.0) was used to perform data quality control, normalization, principal components analysis and uniform manifold approximation and projection (UMAP method). Briefly, cells with fewer than 200 or more than 2,500 unique feature counts, or more than 7% mitochondrial counts were considered low quality cells and removed from further analysis. Then global-scaling method “LogNormalize” was used to normalize the feature expression. A total of 2,000 top variable features were identified by function FindVariableFeatures and selected for subsequent principal components analysis. Top 20 significant components were chosen to conduct cell clustering by using the algorithm

of uniform manifold approximation and projection (UMAP) with default settings. The expression level and feature of selected genes were profiled and visualize by R package ggplot2 (version 3.3.2).

Western blot analysis—P22 lung tissues were collected in RIPA buffer supplemented with Complete Protease Inhibitor Cocktail tablets (Roche) and PhosSTOP Phosphatase Inhibitor Cocktail tablets (Roche). Protein samples were then homogenized in a QIAGEN TissueLyser II. Protein concentrations were measured by Pierce™ BCA Protein Assay kit (Thermo Scientific).

An estimated ~10ug protein sample was loaded in each well and ran on a 4%–12% SDS-PAGE gel (Invitrogen), followed by transfer to PVDF membranes. PVDF membranes were blocked in TBST (0.1% Tween-20) with 5% BSA for 1.5 hours, incubated in primary antibodies overnight, and then incubated in the secondary antibody for 1 hour. All imaging and quantification were performed using the Image Studio Lite software system (LI-COR Biosciences). The following primary antibodies were used: CLDN5 (Invitrogen, 4C3C2, 1:2000), CDH5 (BD, 11D4.1, 1:1500) and β-actin (Novus Biologicals, NB600501, 1:5000). The secondary antibody used were: IRDye 680RD donkey anti–mouse IgG (LI-COR, 925–69072, 1:10,000) and IRDye 680LT goat anti-rat IgG (LI-COR, 925–68029, 1:10,000). Three biological replicates were performed for each antibody.

Evans Blue dye assay—Mice were anesthetized via IP injection of xylazine (10 mg/kg) and ketamine (100 mg/kg). Using a syringe with a 30G needle, 100 μl of 0.5 % Evans Blue in PBS was injected into the tail vein. Mice were allowed to recover on a heating pad for 1h and then sacrificed while still under anesthesia. Serum and BAL were collected as previously described (Smith et al., 2019). After BAL collection, lungs were perfused through the right ventricle with 5 ml PBS, harvested, and processed for further analysis *ex vivo*. To extract Evans Blue from lung tissue, tissues were weighed and then incubated in 250 μl formamide at 58°C for 48h.

Evans Blue in serum, lung tissue and BAL fluid was measured at 620nm by spectrophotometry. Evans Blue readings were corrected for contaminating heme in BAL fluid and lung tissue by measuring samples at 740nm and using the correction factor y=1.193x +0.007 as previously described (Moitra et al., 2007). Lung Evans Blue level was normalized to serum Evans Blue level.

Mouse lung angiogram—P22 mice were anesthetized via IP injection of sodium pentobarbital (120 mg/kg). After opening the chest wall, 20 IU heparin was immediately injected to the right ventricles to prevent blood coagulation. A PE-20 tube was then inserted into the main pulmonary artery via the right ventricle. 3 min pulmonary vasculature flush was performed with 37°C PBS via a syringe pump (NE-300, “Just Infusion”™) at 8.660 speed. 0.03~0.04 mL freshly prepared MicrofilVR polymer mixture (MV-122, Flow-Tech Inc.) was then gently instilled at 4.699 speed into the pulmonary vasculature until the dye reached the peripheral brunches. Lungs and hearts were then isolated and kept at 4°C overnight. Dehydration was carried out the next day after a 15 min DPBS wash with 1 hour wash in 50%, 70%, 80%, 95%, 100% and 100% ethanol solutions, respectively. To clear the

lung, ethanol was replaced by 10mL/sample methyl salicylate (SigmaAldrich). All samples were placed on a rotator at room temperature overnight before imaging.

All lungs were imaged by a stereo microscope. To quantify pulmonary vasculature brunches, all brunches were outlined by Adobe Photoshop and further analyzed with ImageJ plug-in "Analyze Skeleton". Unpaired student's *t* test was performed for statistical analysis. More details for mouse lung angiogram analysis could be found in published literature (Xiong et al., 2021; Zhu et al., 2020).

CGRP, BIBN-4096 and Bicuculline intranasal administration—Synthesized CGRP (Sigma-Aldrich C0292) was dissolved and diluted with saline to working concentration. A volume of 10 μl 1pg/ul CGRP was intranasally administrated to pups at P10, P12, P14 and P16. This concentration was calculated based on physiological range measured by BAL ELISA. BIBN-4096 (Fisher Scientific #45–611-0) and Bicuculline (Fisher Scientific #01–305-0) were dissolved in 100% DMSO (Sigma-Aldrich D2650) and further diluted to working solution with saline right before use. A volume of 10ul of either 0.3mg/ml BIBN-4096 or 50uM Bicuculline was intranasally administrated to pups at P10, P12, P14, P16 and P18. These concentrations were selected as previously described (Aubdool et al., 2014; Chintagari and Liu, 2012).

QUANTIFICATION AND STATISTICAL ANALYSIS

Different quantification methods were used based on the nature of the data, as noted in individual method sections. In addition, as noted in Figure Legends, either one-way or two-way ANOVA Tukey's multiple comparisons test or Student's t test was used depending on data type. All statistical analyses were performed using Prism 6 (GraphPad).

Quantitative PCR (qPCR)—Total RNA was extracted from lungs using Trizol (Invitrogen) and RNeasy Mini RNA extraction kit (Qiagen). RT-PCR was then performed to obtain corresponding cDNA using iScript Select cDNA Synthesis Kit (Bio-Rad). qPCR was performed by CFX Connect™ system (Bio-Rad) using SYBR Green (Bio-Rad). At least three technical and three biological replicates were performed for each gene if not otherwise notated. All primers used for qPCR analysis are listed in Table S3.

Supplementary Material

Refer to Web version on PubMed Central for supplementary material.

ACKNOWLEDGMENTS

The authors would like to thank members of the Sun lab for inputs and discussions. This work was supported by NIH R01HL146141 (to X.S. and L.R.Y.), NIH OT2OD023857 (to X.S.), ATS Research Foundation 2019-1059 (to X.S.), Orphan Disease Center MDBR-21-115-NEHI (to X.S. and L.R.Y) and AHA predoctoral fellowship 828448 (to J.X.). Single cell RNA-seq was performed using the service of UC San Diego IGM Genomics Center utilizing an Illumina NovaSeq 6000 that was purchased with funding from a National Institutes of Health SIG grant (#S10 OD026929). Cell sorting was performed using the Flow Cytometry Core at the San Diego Center for AIDS Research (P30 AI036214), the VA San Diego Health Care System, and the San Diego Veterans Medical Research Foundation. We also thank the UCSD School of Medicine Microscopy Core (National Institute of Neurological Disorders and Stroke Grant P30 NS047101) for assistance with imaging and analysis.

REFERENCES

Ackermann M, Verleden SE, Kuehnel M, Haverich A, Welte T, Laenger F, Vanstapel A, Werlein C, Stark H, Tzankov A, et al. (2020). Pulmonary Vascular Endothelialitis, Thrombosis, and Angiogenesis in Covid-19. N Engl J Med 383, 120–128. [PubMed: 32437596]

Aiyar N, Rand K, Elshourbagy NA, Zeng Z, Adamou JE, Bergsma DJ, and Li Y (1996). A cDNA encoding the calcitonin gene-related peptide type 1 receptor. J Biol Chem 271, 11325–11329. [PubMed: 8626685]

Aubdool AA, Graepel R, Kodji X, Alawi KM, Bodkin JV, Srivastava S, Gentry C, Heads R, Grant AD, Fernandes ES, et al. (2014). TRPA1 is essential for the vascular response to environmental cold exposure. Nat Commun 5, 5732. [PubMed: 25501034]

Baral P, Umans BD, Li L, Wallrapp A, Bist M, Kirschbaum T, Wei Y, Zhou Y, Kuchroo VK, Burkett PR, et al. (2018). Nociceptor sensory neurons suppress neutrophil and gammadelta T cell responses in bacterial lung infections and lethal pneumonia. Nat Med 24, 417–426. [PubMed: 29505031]

Barrios J, Kho AT, Aven L, Mitchel JA, Park JA, Randell SH, Miller LA, Tantisira KG, and Ai X (2019). Pulmonary Neuroendocrine Cells Secrete gamma-Aminobutyric Acid to Induce Goblet Cell Hyperplasia in Primate Models. Am J Respir Cell Mol Biol 60, 687–694. [PubMed: 30571139]

Barrios J, Patel KR, Aven L, Achey R, Minns MS, Lee Y, Trinkaus-Randall VE, and Ai X (2017). Early life allergen-induced mucus overproduction requires augmented neural stimulation of pulmonary neuroendocrine cell secretion. FASEB J 31, 4117–4128. [PubMed: 28566470]

Brain S, Williams T, Tippins J, Morris H, and MacIntyre I (1985). Calcitonin gene-related peptide is a potent vasodilator. Nature 313, 54–56. [PubMed: 3917554]

Brain SD, and Grant AD (2004). Vascular actions of calcitonin gene-related peptide and adrenomedullin. Physiol Rev 84, 903–934. [PubMed: 15269340]

Breen ID, Brumfiel CM, Patel MH, Butterfield RJ, VanderPluym JH, Griffing L, Pittelkow MR, and Mangold AR (2021). Evaluation of the Safety of Calcitonin Gene-Related Peptide Antagonists for Migraine Treatment Among Adults With Raynaud Phenomenon. JAMA Netw Open 4, e217934. [PubMed: 33871613]

Chintagari NR, and Liu L (2012). GABA receptor ameliorates ventilator-induced lung injury in rats by improving alveolar fluid clearance. Crit Care 16, R55. [PubMed: 22480160]

Cutz E, Yeger H, and Pan J (2007). Pulmonary neuroendocrine cell system in pediatric lung disease-recent advances. Pediatr Dev Pathol 10, 419–435. [PubMed: 18001162]

D'Agnillo F, Walters KA, Xiao Y, Sheng ZM, Scherler K, Park J, Gygli S, Rosas LA, Sadtler K, Kalish H, et al. (2021). Lung epithelial and endothelial damage, loss of tissue repair, inhibition of fibrinolysis, and cellular senescence in fatal COVID-19. Sci Transl Med 13, eabj7790. [PubMed: 34648357]

Deterding RR, Pye C, Fan LL, and Langston C (2005). Persistent tachypnea of infancy is associated with neuroendocrine cell hyperplasia. Pediatr Pulmonol 40, 157–165. [PubMed: 15965897]

Domyan ET, Ferretti E, Throckmorton K, Mishina Y, Nicolis SK, and Sun X (2011). Signaling through BMP receptors promotes respiratory identity in the foregut via repression of Sox2. Development 138, 971–981. [PubMed: 21303850]

Du Y, Kitzmiller JA, Sridharan A, Perl AK, Bridges JP, Misra RS, Pryhuber GS, Mariani TJ, Bhattacharya S, Guo M, et al. (2017). Lung Gene Expression Analysis (LGEA): an integrative web portal for comprehensive gene expression data analysis in lung development. Thorax 72, 481–484. [PubMed: 28070014]

Espiritu RF, Pittet JF, Matthay MA, and Goetzl EJ (1992). Neuropeptides in pulmonary edema fluid of adult respiratory distress syndrome. Inflammation 16, 509–517. [PubMed: 1428125]

Fox SE, Akmatbekov A, Harbert JL, Li G, Quincy Brown J, and Vander Heide RS (2020). Pulmonary and cardiac pathology in African American patients with COVID-19: an autopsy series from New Orleans. The Lancet Respiratory Medicine 8, 681–686. [PubMed: 32473124]

Fritz-Six KL, Dunworth WP, Li M, and Caron KM (2008). Adrenomedullin signaling is necessary for murine lymphatic vascular development. J Clin Invest 118, 40–50. [PubMed: 18097475]

Gotts JE, Bernard O, Chun L, Croze RH, Ross JT, Nesseler N, Wu X, Abbott J, Fang X, Calfee CS, et al. (2019). Clinically relevant model of pneumococcal pneumonia, ARDS, and nonpulmonary

organ dysfunction in mice. Am J Physiol Lung Cell Mol Physiol 317, L717–L736. [PubMed: 31509438]

Hennessy ML, Corcoran AE, Brust RD, Chang Y, Nattie EE, and Dymecki SM (2017). Activity of Tachykinin1-Expressing Pet1 Raphe Neurons Modulates the Respiratory Chemoreflex. J Neurosci 37, 1807–1819. [PubMed: 28073937]

Huppert LA, Matthay MA, and Ware LB (2019). Pathogenesis of Acute Respiratory Distress Syndrome. Semin Respir Crit Care Med 40, 31–39. [PubMed: 31060086]

Ito T, Udaka N, Yazawa T, Okudela K, Hayashi H, Sudo T, Guillemot F, Kageyama R, and Kitamura H (2000). Basic helix-loop-helix transcription factors regulate the neuroendocrine differentiation of fetal mouse pulmonary epithelium. Development 127, 3913–3921. [PubMed: 10952889]

Jang AS, Concel VJ, Bein K, Brant KA, Liu S, Pope-Varsalona H, Dopico RA Jr., Di YP, Knoell DL, Barchowsky A, et al. (2011). Endothelial dysfunction and claudin 5 regulation during acrolein-induced lung injury. Am J Respir Cell Mol Biol 44, 483–490. [PubMed: 20525806]

Jin S, Guerrero-Juarez CF, Zhang L, Chang I, Ramos R, Kuan CH, Myung P, Plikus MV, and Nie Q (2021). Inference and analysis of cell-cell communication using CellChat. Nat Commun 12, 1088. [PubMed: 33597522]

Kaelberer MM, Buchanan KL, Klein ME, Barth BB, Montoya MM, Shen X, and Bohorquez DV (2018). A gut-brain neural circuit for nutrient sensory transduction. Science 361.

Kuo CS, and Krasnow MA (2015). Formation of a Neurosensory Organ by Epithelial Cell Slithering. Cell 163, 394–405. [PubMed: 26435104]

Kusakabe T, Kawaguchi A, Hoshi N, Kawaguchi R, Hoshi S, and Kimura S (2006). Thyroid-specific enhancer-binding protein/NKX2.1 is required for the maintenance of ordered architecture and function of the differentiated thyroid. Mol Endocrinol 20, 1796–1809. [PubMed: 16601074]

Li C, Li A, Xing Y, Li M, Chan B, Ouyang R, Taketo MM, Kucherlapati R, Borok Z, and Minoo P (2013). Apc deficiency alters pulmonary epithelial cell fate and inhibits Nkx2.1 via triggering TGF-beta signaling. Dev Biol 378, 13–24. [PubMed: 23562608]

Liptzin DR, Pickett K, Brinton JT, Agarwal A, Fishman MP, Casey A, Towe CT, Taylor JB, Kurland G, Hagood JS, et al. (2020). Neuroendocrine Cell Hyperplasia of Infancy. Clinical Score and Comorbidities. Ann Am Thorac Soc 17, 724–728. [PubMed: 32109152]

MaassenVanDenBrink A, Meijer J, Villalon CM, and Ferrari MD (2016). Wiping Out CGRP: Potential Cardiovascular Risks. Trends Pharmacol Sci 37, 779–788. [PubMed: 27338837]

Matthay MA, Zemans RL, Zimmerman GA, Arabi YM, Beitler JR, Mercat A, Herridge M, Randolph AG, and Calfee CS (2019). Acute respiratory distress syndrome. Nat Rev Dis Primers 5, 18. [PubMed: 30872586]

Minoo P, Su G, Drum H, Bringas P, and Kimura S (1999). Defects in tracheoesophageal and lung morphogenesis inNkx2. 1 (−/−) mouse embryos. Developmental biology 209, 60–71. [PubMed: 10208743]

Moitra J, Sammani S, and Garcia JG (2007). Re-evaluation of Evans Blue dye as a marker of albumin clearance in murine models of acute lung injury. Transl Res 150, 253–265. [PubMed: 17900513]

Nevel RJ, Garnett ET, Schaudies DA, and Young LR (2018). Growth trajectories and oxygen use in neuroendocrine cell hyperplasia of infancy. Pediatr Pulmonol 53, 656–663. [PubMed: 29393588]

Newbold P, and Brain SD (1993). The modulation of inflammatory oedema by calcitonin gene-related peptide. Br J Pharmacol 108, 705–710. [PubMed: 7682134]

Ochs M, Nyengaard JR, Jung A, Knudsen L, Voigt M, Wahlers T, Richter J, and Gundersen HJ (2004). The number of alveoli in the human lung. Am J Respir Crit Care Med 169, 120–124. [PubMed: 14512270]

Olesen J, Diener HC, Husstedt IW, Goadsby PJ, Hall D, Meier U, Pollentier S, Lesko LM, and Group B.B.C.P.o.C.S. (2004). Calcitonin gene-related peptide receptor antagonist BIBN 4096 BS for the acute treatment of migraine. N Engl J Med 350, 1104–1110. [PubMed: 15014183]

Pacary E, Heng J, Azzarelli R, Riou P, Castro D, Lebel-Potter M, Parras C, Bell DM, Ridley AJ, Parsons M, et al. (2011). Proneural transcription factors regulate different steps of cortical neuron migration through Rnd-mediated inhibition of RhoA signaling. Neuron 69, 1069–1084. [PubMed: 21435554]

Perrot CY, Sawada J, and Komatsu M (2018). Prolonged activation of cAMP signaling leads to endothelial barrier disruption via transcriptional repression of RRAS. FASEB J, fj201700818RRR.

Que J, Okubo T, Goldenring JR, Nam KT, Kurotani R, Morrisey EE, Taranova O, Pevny LH, and Hogan BL (2007). Multiple dose-dependent roles for Sox2 in the patterning and differentiation of anterior foregut endoderm. Development 134, 2521–2531. [PubMed: 17522155]

Schneider CA, Rasband WS, and Eliceiri KW (2012). NIH Image to ImageJ: 25 years of image analysis. Nature methods 9, 671–675. [PubMed: 22930834]

Smith P, Jeffers LA, and Koval M (2019). Effects of different routes of endotoxin injury on barrier function in alcoholic lung syndrome. Alcohol 80, 81–89. [PubMed: 31278041]

Su Y, Barr J, Jaquish A, Xu J, Verheyden JM, and Sun X (2022). Identification of lung innervating sensory neurons and their target specificity. Am J Physiol Lung Cell Mol Physiol 322, L50–L63. [PubMed: 34755535]

Sui P, Wiesner DL, Xu J, Zhang Y, Lee J, Van Dyken S, Lashua A, Yu C, Klein BS, Locksley RM, et al. (2018). Pulmonary neuroendocrine cells amplify allergic asthma responses. Science 360.

Taddei A, Giampietro C, Conti A, Orsenigo F, Breviario F, Pirazzoli V, Potente M, Daly C, Dimmeler S, and Dejana E (2008). Endothelial adherens junctions control tight junctions by VE-cadherin-mediated upregulation of claudin-5. Nat Cell Biol 10, 923–934. [PubMed: 18604199]

Travaglini KJ, Nabhan AN, Penland L, Sinha R, Gillich A, Sit RV, Chang S, Conley SD, Mori Y, Seita J, et al. (2020). A molecular cell atlas of the human lung from single-cell RNA sequencing. Nature 587, 619–625. [PubMed: 33208946]

Wang A, Chiou J, Poirion OB, Buchanan J, Valdez MJ, Verheyden JM, Hou X, Kudtarkar P, Narendra S, Newsome JM, et al. (2020). Single-cell multiomic profiling of human lungs reveals cell-type-specific and age-dynamic control of SARS-CoV2 host genes. Elife 9.

Xiang YY, Wang S, Liu M, Hirota JA, Li J, Ju W, Fan Y, Kelly MM, Ye B, Orser B, et al. (2007). A GABAergic system in airway epithelium is essential for mucus overproduction in asthma. Nat Med 13, 862–867. [PubMed: 17589520]

Xiong M, Jain PP, Chen J, Babicheva A, Zhao T, Alotaibi M, Kim NH, Lai N, Izadi A, Rodriguez M, et al. (2021). Mouse model of experimental pulmonary hypertension: Lung angiogram and right heart catheterization. Pulm Circ 11, 20458940211041512. [PubMed: 34531976]

Xu J, Yu H, and Sun X (2020). Less Is More: Rare Pulmonary Neuroendocrine Cells Function as Critical Sensors in Lung. Dev Cell 55, 123–132. [PubMed: 33108755]

Xu X, Huang L, Futtner C, Schwab B, Rampersad RR, Lu Y, Sporn TA, Hogan BL, and Onaitis MW (2014). The cell of origin and subtype of K-Ras-induced lung tumors are modified by Notch and Sox2. Genes Dev 28, 1929–1939. [PubMed: 25184679]

Young LR, Brody AS, Inge TH, Acton JD, Bokulic RE, Langston C, and Deutsch GH (2011). Neuroendocrine cell distribution and frequency distinguish neuroendocrine cell hyperplasia of infancy from other pulmonary disorders. Chest 139, 1060–1071. [PubMed: 20884725]

Young LR, Deutsch GH, Bokulic RE, Brody AS, and Nogee LM (2013). A mutation in TTF1/NKX2.1 is associated with familial neuroendocrine cell hyperplasia of infancy. Chest 144, 1199–1206. [PubMed: 23787483]

Zhu Z, Wang Y, Long A, Feng T, Ocampo M, Chen S, Tang H, Guo Q, Minshall R, Makino A, et al. (2020). Pulmonary vessel casting in a rat model of monocrotaline-mediated pulmonary hypertension. Pulm Circ 10, 2045894020922129. [PubMed: 32922742]

Highlights:

- Increased PNECs are responsible for poor gas exchange in a NEHI mouse model
- Increased PNECs and CGRP led to impaired endothelial barrier and excess fluid
- Antagonizing CGRP signaling improved barrier and oxygenation in NEHI mouse mutants
- Increased neuropeptides and reduced endothelial junctions were found in ARDS lungs

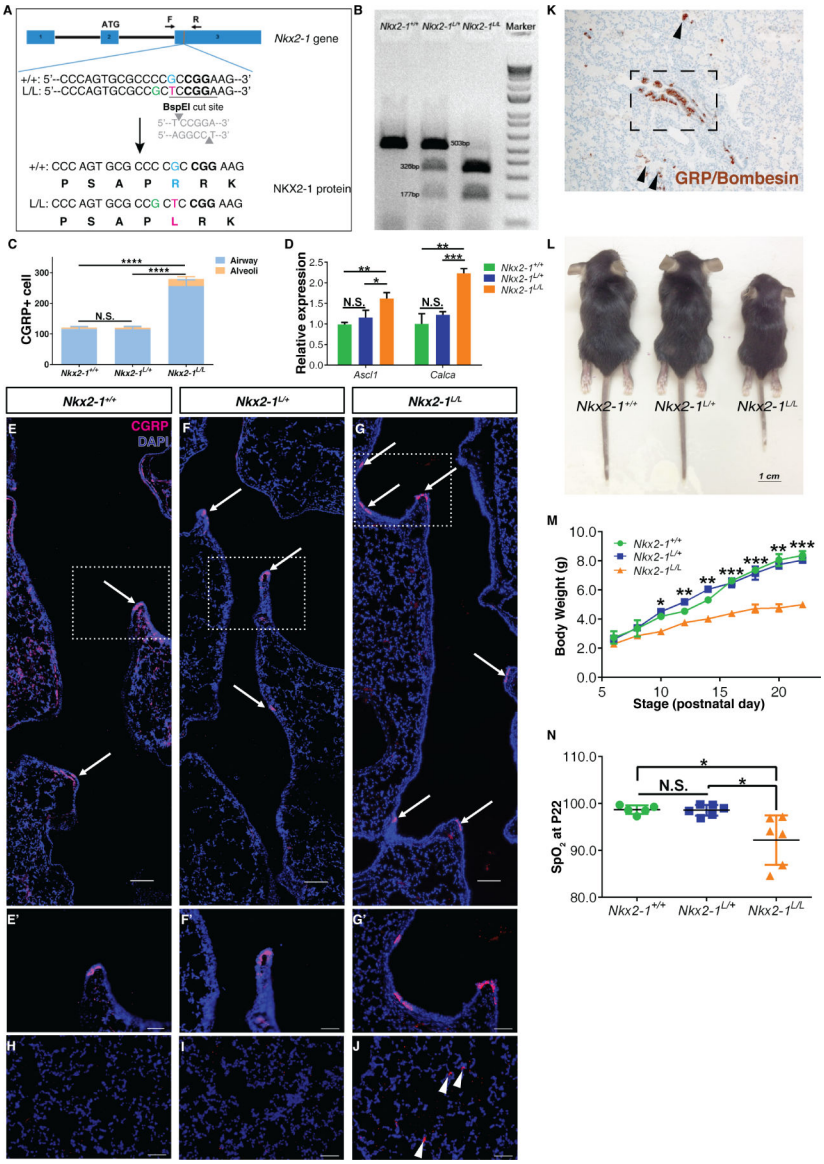

Figure 1. Establishing the *Nkx2–1* Mutant Model of NEHI using CRISPR/Cas9 Genome Editing.

(A) Schematic of CRISPR/Cas9 strategy to generate *Nkx2–1*^{R161L} (*Nkx2–1*^{L}) allele. Aside from engineered changes, a silent C→G change also arose in the CRISPR/Cas9 repair process, and is noted in green.

(B) RFLP-based genotyping. Introduction of BspEI site in the mutant allele led to digestion of 503bp PCR product into 326bp and 177bp fragments.

(C) PNEC quantification of whole left lobe at E18.5 (n=3 for each group), statistical analysis was performed on total PNEC number (airway and alveoli combined).

(D) qPCR of PNEC markers *Ascl1* and *Calca* at P22 (n=3 for each group). (E-G) Representative longitudinal section of the main airway in P22 lung for each group with anti-CGRP staining labeling PNECs (arrows). Scale bar: 100μm.

(E'-G') Magnified view of boxed areas in E-G, respectively. Scale bar: 50μm. (H-J) CGRP+ cells (arrowheads) were ectopically detected in the alveolar region of *Nkx2–1*$^{L/L}$ mutants. Scale bar: 50μm.

(K) NEHI patient biopsy with anti-GRP/Bombesin labeling of PNECs showing large NEB at bronchiole (dashed box) and ectopic solitary PNECs in alveolar region (arrowheads).

(L) Representative body size at P22.

(M) Growth curve from P5 to P22 of 12 pups nursed by the same outbred foster mother (n=4 for each group). Statistical analysis was carried out separately at each time point.

(N)Oxygen saturation at P22 (n≥6 for each group). One-way ANOVA Tukey's multiple comparisons test was used for C, D, M and N. N.S. not significant, p≥0.05. * for p<0.05, ** for p<0.01, *** for p<0.001. Error bars represent means ± SD.

See also Figure S1.

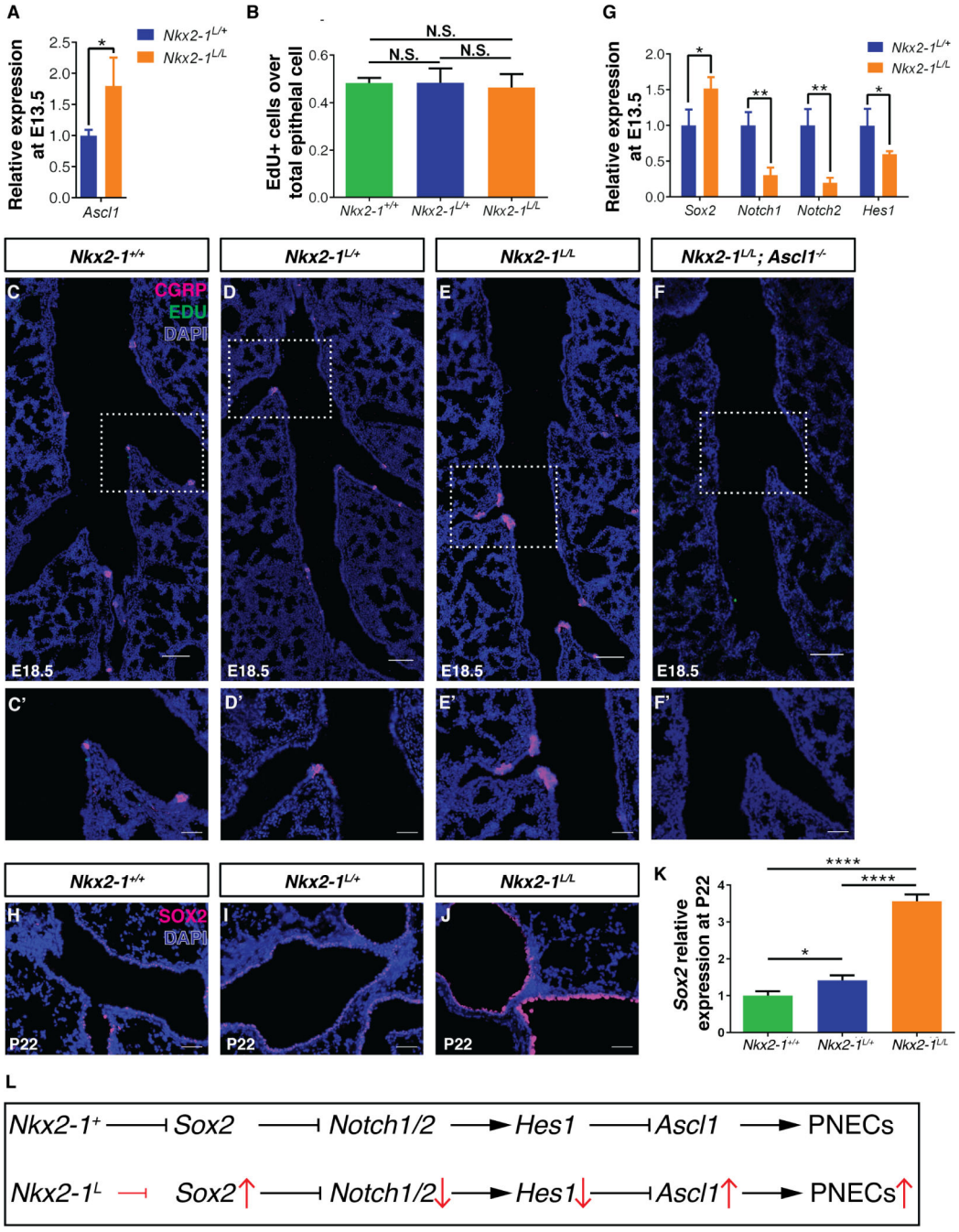

Figure 2. PNEC Hyperplasia in *Nkx2–1*$^{L/L}$ Mutants is Associated with Increased *Sox2*, Decreased Notch Signaling and Increased Specification rather than Proliferation.

(A) qPCR showing increased PNEC marker *Ascl1* at E13.5 when PNECs are first specified (n=3 for each group).

(B) Rate of epithelial cell proliferation quantified by EdU staining at E13.5 (n=3 for each group).

(C-F) Representative longitudinal section of the main airway of E18.5 lungs with anti-CGRP antibody staining labeling PNECs. Scale bar: 100μm.

(C'-F') Magnified view of boxed areas in C-F, respectively. Scale bar: 50μm.

(G) qPCR of *Sox2* and Notch pathway genes *Notch1*, *Notch2* and *Hes1* at E13.5 (n=3 for each group).
(H-J) Representative anti-SOX2 antibody staining at P22. Scale bar: 100μm.
(K) qPCR of *Sox2* at P22 (n=3 for each group).
(L) Schematics of a molecular mechanism linking *Nkx2–1*^{L} mutation to PNEC hyperplasia, as supported by data here and previous publications (Domyan et al., 2011; Ito et al., 2000; Li et al., 2013; Que et al., 2007; Xu et al., 2014).
Student's *t* test was used for A and K. One-way ANOVA Tukey's multiple comparisons test was used for B and K. N.S. not significant, $p \geq 0.05$. * for $p < 0.05$, ** for $p < 0.01$, **** for $p < 0.0001$. Error bars represent means ± SD.
See also Figure S2.

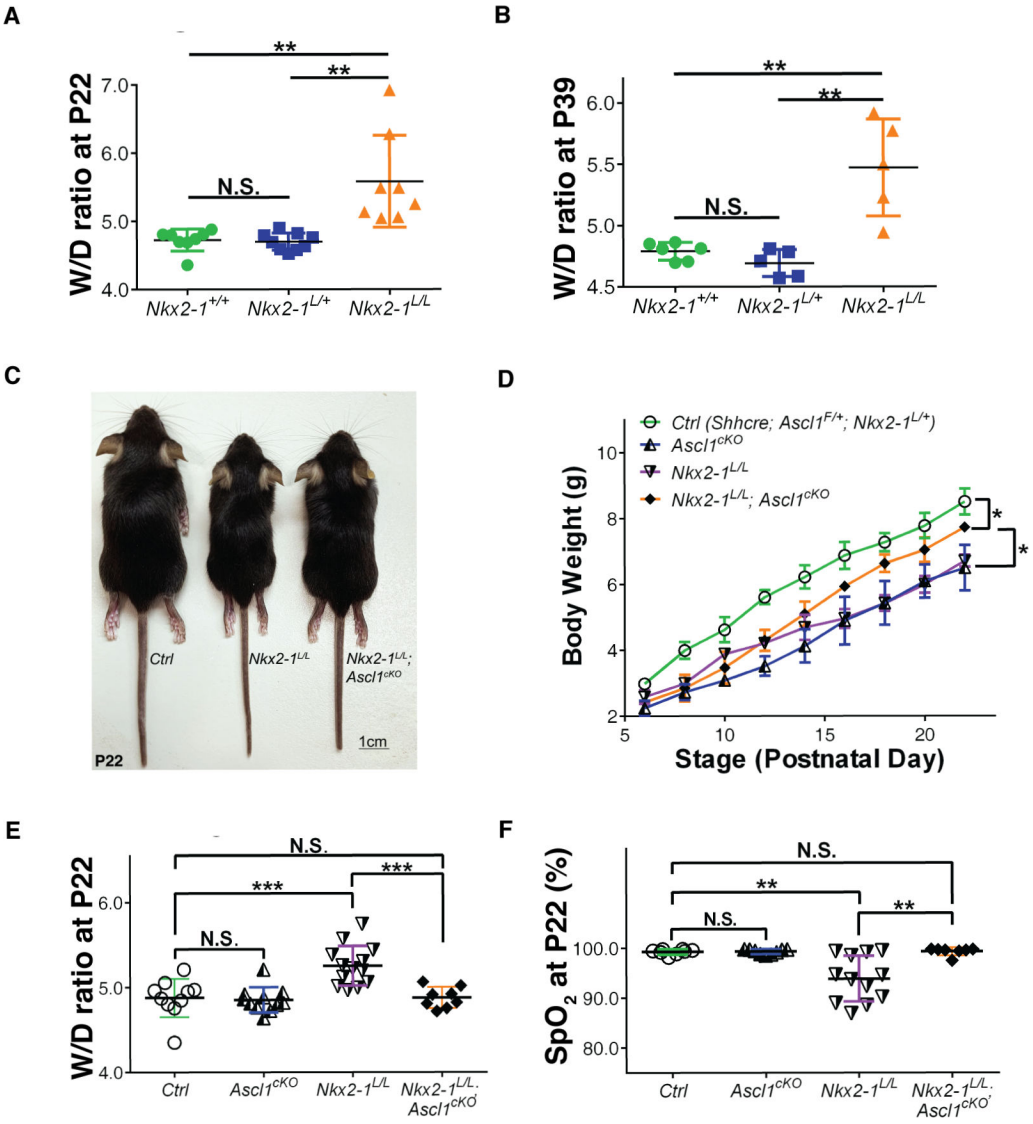

Figure 3. PNEC Hyperplasia is Responsible for Lung Fluid Increase and Gas Exchange Deficiency.

(A, B) Lung W/D ratio at P22 (n≥8 for each group) and at P39 (n≥5 for each group).

(C) Representative body size at P22.

(D) Growth curve from P5 to P22 of 12 pups nursed by the same outbred foster mother (n=3 for each group). Statistical analysis was carried out separately at each time point.

(E) Lung W/D ratio at P22 (n≥8 for each group).

(F) Oxygen saturation as measured by SpO_2 at P22 (n≥7 for each group). One-way ANOVA Tukey's multiple comparisons test was used for A, B and two-way ANOVA Tukey's multiple comparisons test was used for D-F. N.S. not significant, * for $p<0.05$, ** for $p<0.01$, *** for $p<0.001$. Error bars represent means ± SD.

See also Figure S3.

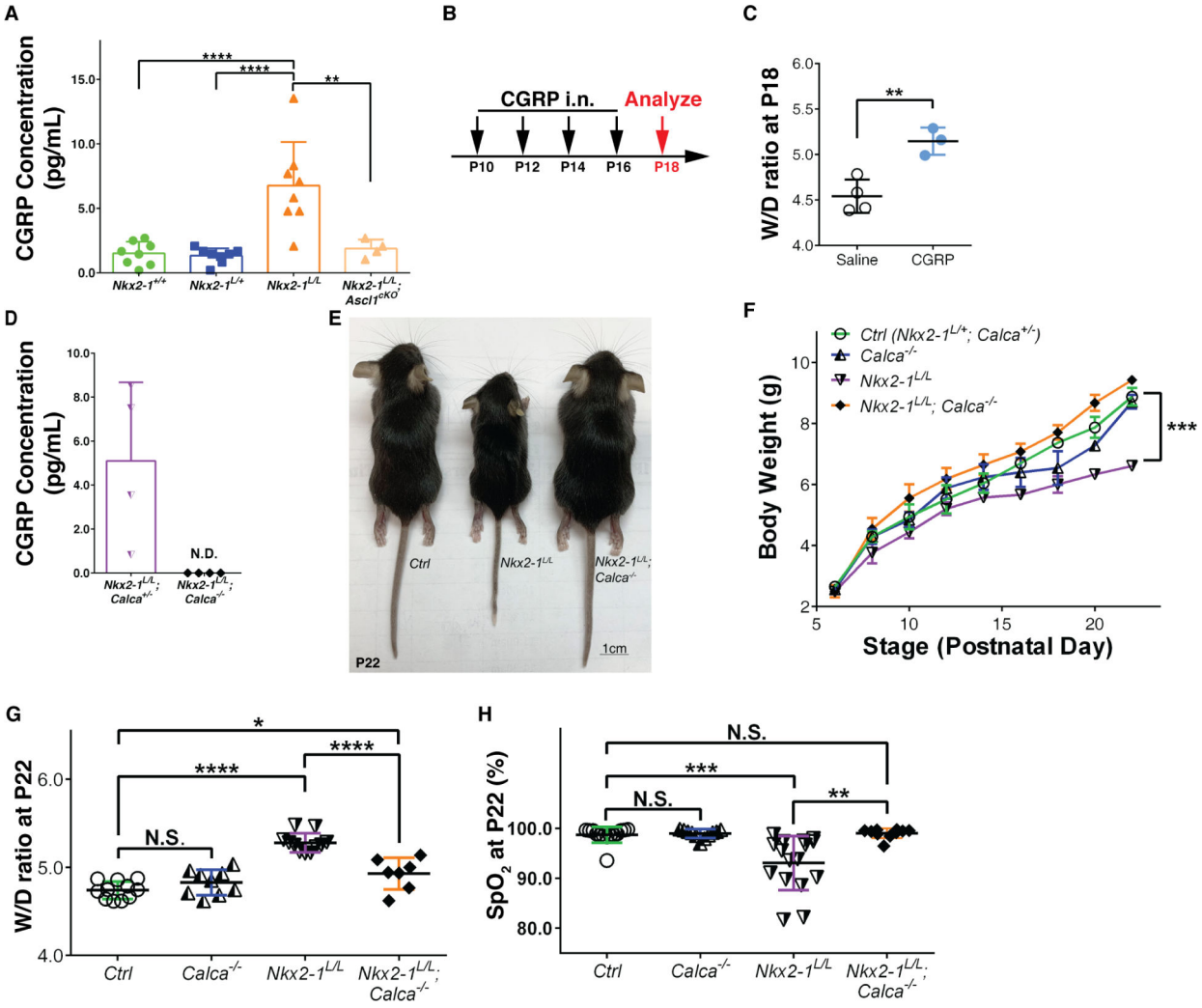

Figure 4. PNEC Product CGRP Contributed to Lung Fluid Increase and Gas Exchange Deficiency.

(A) CGRP concentration in BAL as measured by ELISA for each genotype (n=8 for first three groups, n=4 for *Nkx2–1*$^{L/L}$; *Ascl1*^{cKO} mutants).

(B) Wild-type mice were intranasally administrated with 10μl 1pg/μl CGRP or saline at P10, P12, P14 and P16. This concentration was selected based on physiological range measured by BAL ELISA.

(C) Lung W/D ratio measured at P18 (n=4 for saline-treated group, n=3 for CGRP-treated group).

(D) CGRP concentration in BAL as measured by ELISA for each genotype (n=4 for each group).

(E) Representative body size at P22.

(F) Growth curve from P5 to P22 of 12 pups nursed by the same outbred foster mother (n=3 for each group). Statistical analysis was carried out separately at each time point.

(G) Lung W/D ratio at P22 (n≥7 for each group).

(H) Oxygen saturation at P22 (n≥10 for each group).

One-way ANOVA Tukey's multiple comparisons test was used for A. Student's *t* test was used for C, and two-way ANOVA Tukey's multiple comparisons test was used for F-H. N.S. not significant, $p \geq 0.05$. * for $p < 0.05$, ** for $p < 0.01$, *** for $p < 0.001$, **** for $p < 0.0001$. Error bars represent means ± SD.

See also Figure S4.

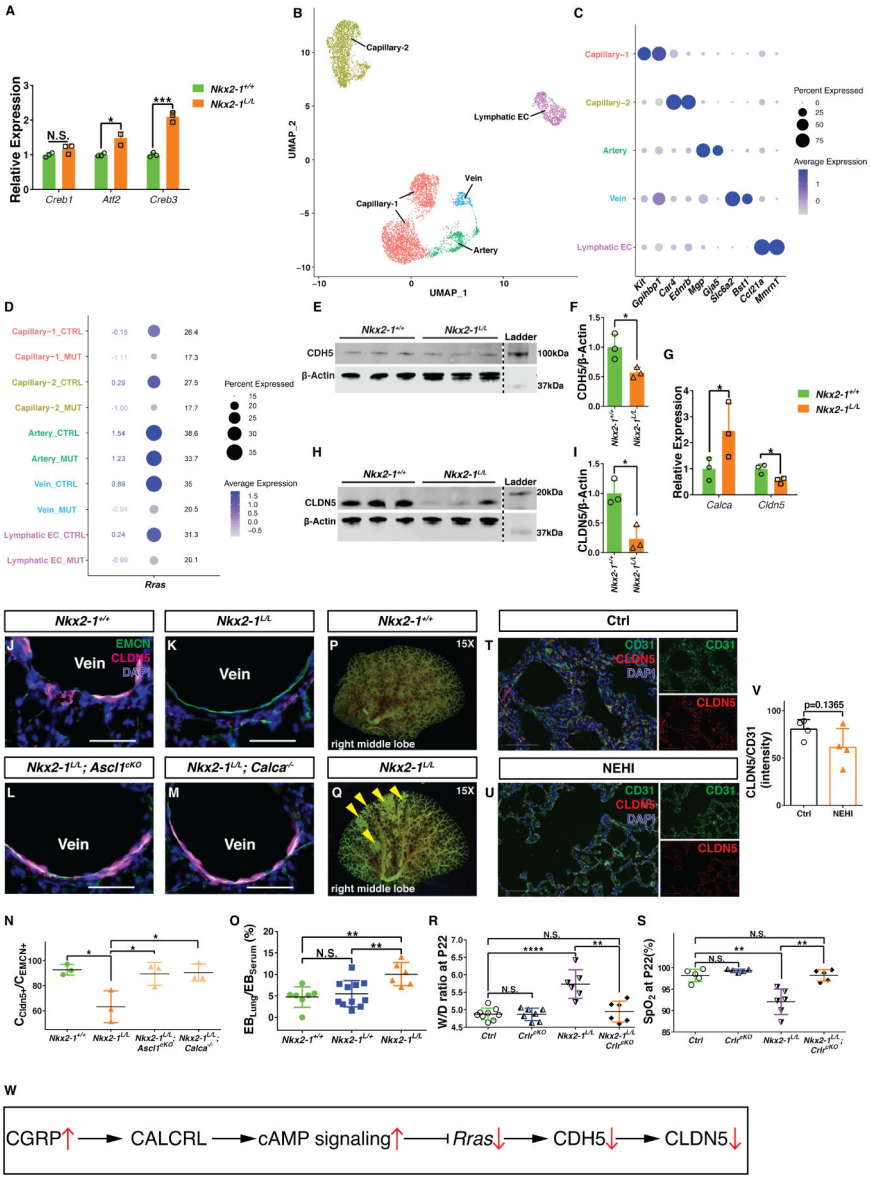

Figure 5. Excess CGRP Produced by PNECs Signals to Pulmonary Endothelial Cells and in turn Leads to Excess Fluid and Reduced Oxygenation in the NEHI Mouse Model.

(A) qPCR of CGRP downstream cAMP signaling genes *Creb1*, *Atf2* (also termed *Creb2*) and *Creb3* in P22 whole lungs (n=3 for each group).

(B) Integrated uniform manifold approximation and projection (UMAP) plot of scRNA-seq data of CD31+ endothelial cells isolated from P22 *Nkx2–1*$^{+/+}$ and *Nkx2–1*$^{L/L}$ lungs.

(C) Dot plot showing marker genes for each population.

(D) Dot plot of *Rras* expression in individual endothelial population showing a decrease in vein, lymphatics and both capillary populations in the Mut (*Nkx2–1*$^{L/L}$) compared to Ctrl (*Nkx2–1*$^{+/+}$) lungs. Numbers on the left denote expression levels while numbers on the right denote percentages of cells within each equivalent cell types expressing *Cldn5*. (E) CDH5 protein level as assayed by western blot of P22 lungs. Dashed line denotes a cut from the original blot.

(F) Quantification of CDH5 protein level after normalization to internal control beta-actin level (n=3 for each group).
(G) qRT-PCR confirming increased *Calca* and showing decreased *Cldn5* in P22 mutant versus control lungs.
(H) CLDN5 protein level assayed by western blot of P22 lungs. Dashed line denotes a cut from the original blot.
(I) Quantification of CLDN5 protein level in whole lungs after normalization to internal control beta-actin level (n=3 for each group).
(J-M) Anti-CLDN5 antibody staining (magenta) and anti-EMCN antibody staining for vein cells (green) showed reduced CLDN5 expression in $Nkx2\text{–}1^{L/L}$ mutants compared to $Nkx2\text{–}1^{+/+}$ controls (J, K). $Nkx2\text{–}1^{L/L}; Ascl1^{cKO}$ and $Nkx2\text{–}1^{L/L}; Calca^{-/-}$ compound mutants showed similar CLDN5 pattern as $Nkx2\text{–}1^{+/+}$ controls (L, M). Scale bar: 50μm. (N) Percentage of the vessel circumference outlined by EMCN staining that was also CLDN5+ (n=3 for each group).
(O) Lung Evans Blue level as a ratio of dye retained in lung versus level in serum (n≥6 for each group).
(P, Q) Representative whole mount angiogram images of right middle lobes of $Nkx2\text{–}1^{+/+}$ (P) and $Nkx2\text{–}1^{L/L}$ (Q) mice at P22 where leakage was observed in the mutant lung. Magnification: 15X. Leaking regions were marked by yellow arrowheads in Q.
(R) Lung W/D ratio at P22 (n≥6 for each group).
(S) Oxygen saturation at P22 (n≥5 for each group).
(T, U) Representative anti-CD31 antibody (green) and anti-CLDN5 antibody double staining (red) showed a decrease of CLDN5 in human NEHI patient biopsies (U) compared to normal lung biopsies (T). Scale bar: 100μm.
(V) CLDN5/CD31 intensity ratio showing a trending decrease of ratio in NEHI biopsies compared to control (n=4 for each group).
(R) Schematics of a molecular mechanism linking increased CGRP and disrupted endothelial integrity in $Nkx2\text{–}1^{L/L}$ mutants, as supported by data here and previous publications (Aiyar et al., 1996; Jang et al., 2011; Perrot et al., 2018; Taddei et al., 2008; Travaglini et al., 2020; Wang et al., 2020).
Student's *t* test was used for A, F, G, I and V. One-way ANOVA Tukey's multiple comparisons test was used for N and O. Two-way ANOVA Tukey's multiple comparisons test was used for R and S. N.S. not significant, p≥0.05. ** for p<0.05, ** for p<0.01, *** for p<0.001, **** for p<0.0001. Error bars represent means ± SD.
See also Figure S5 and Table S1.

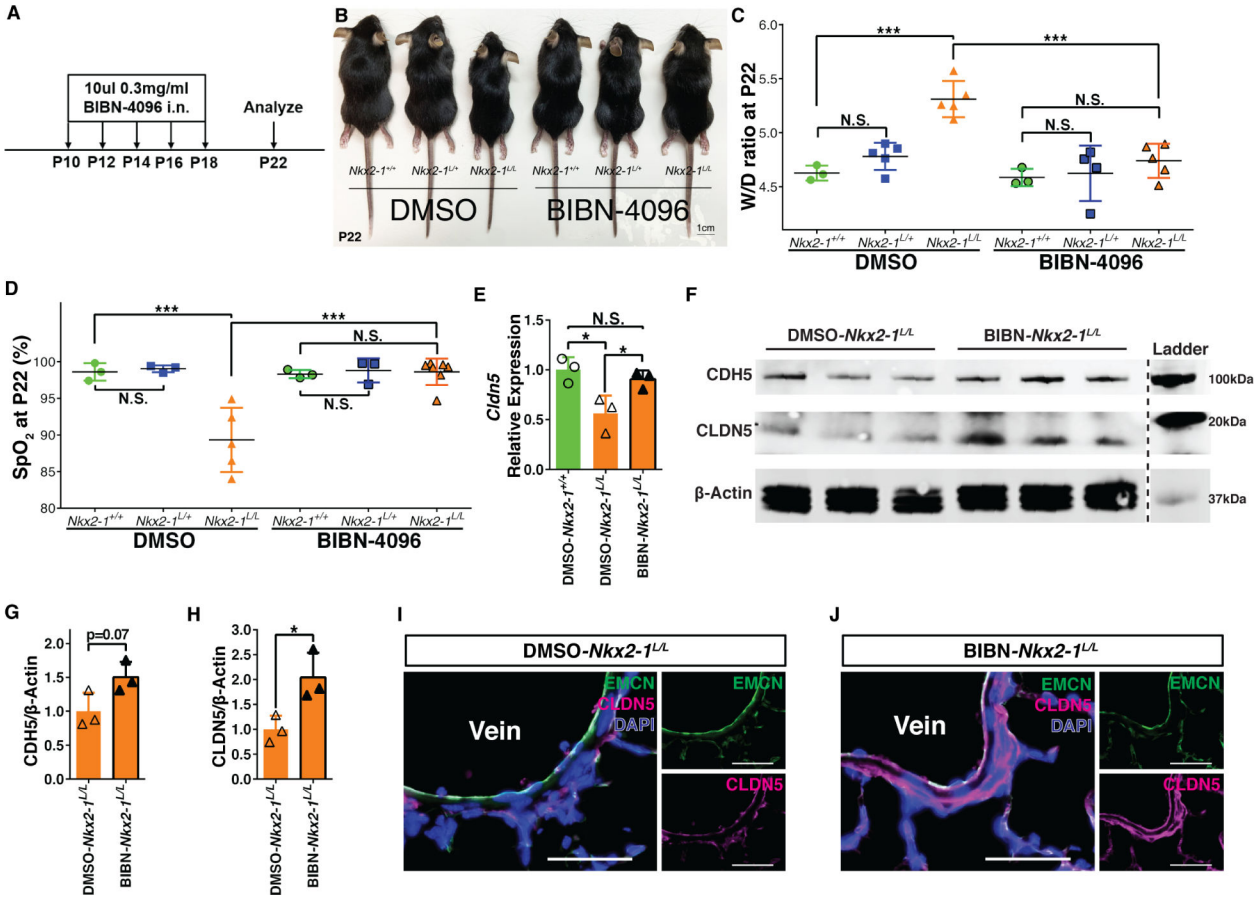

Figure 6. Antagonizing CGRP Signaling Reversed Molecular Changes, Alleviated Excess Fluid and Reduced Oxygenation in the NEHI Mouse Model.

(A) Regime of intranasal BIBN-4096 administration. The dose was selected based on published literature (Aubdool et al., 2014).

(B) Representative body size comparison at P22. All individuals were nursed by the same foster mother.

(C) Lung W/D ratio at P22 (n≥3 for each group).

(D) Oxygen saturation at P22 (n≥3 for each group).

(E) qPCR of *Cldn5* at P22, n=3 for each group.

(F-H) CDH5 and CLDN5 protein levels in P22 lungs as assayed by western blot. Dashed line denotes a cut from the original blot. Quantifications were shown in G and H, respectively. n=3 for each group.

(I, J) Representative anti-CLDN5 antibody staining (magenta) and anti-EMCN antibody staining for vein cells (green) showed restored CLDN5 level in BIBN-treated *Nkx2–1*$^{L/L}$ mutants compared to DMSO-treated *Nkx2–1*$^{L/L}$ mutants.

Two-way ANOVA Tukey's multiple comparisons test was used for C and D. One-way ANOVA Tukey's multiple comparisons test was used for E. Student's *t* test was used for G and H. N.S. not significant, p≥0.05. * for p<0.05, *** for p<0.001. Error bars represent means ± SD.

See also Figure S6.

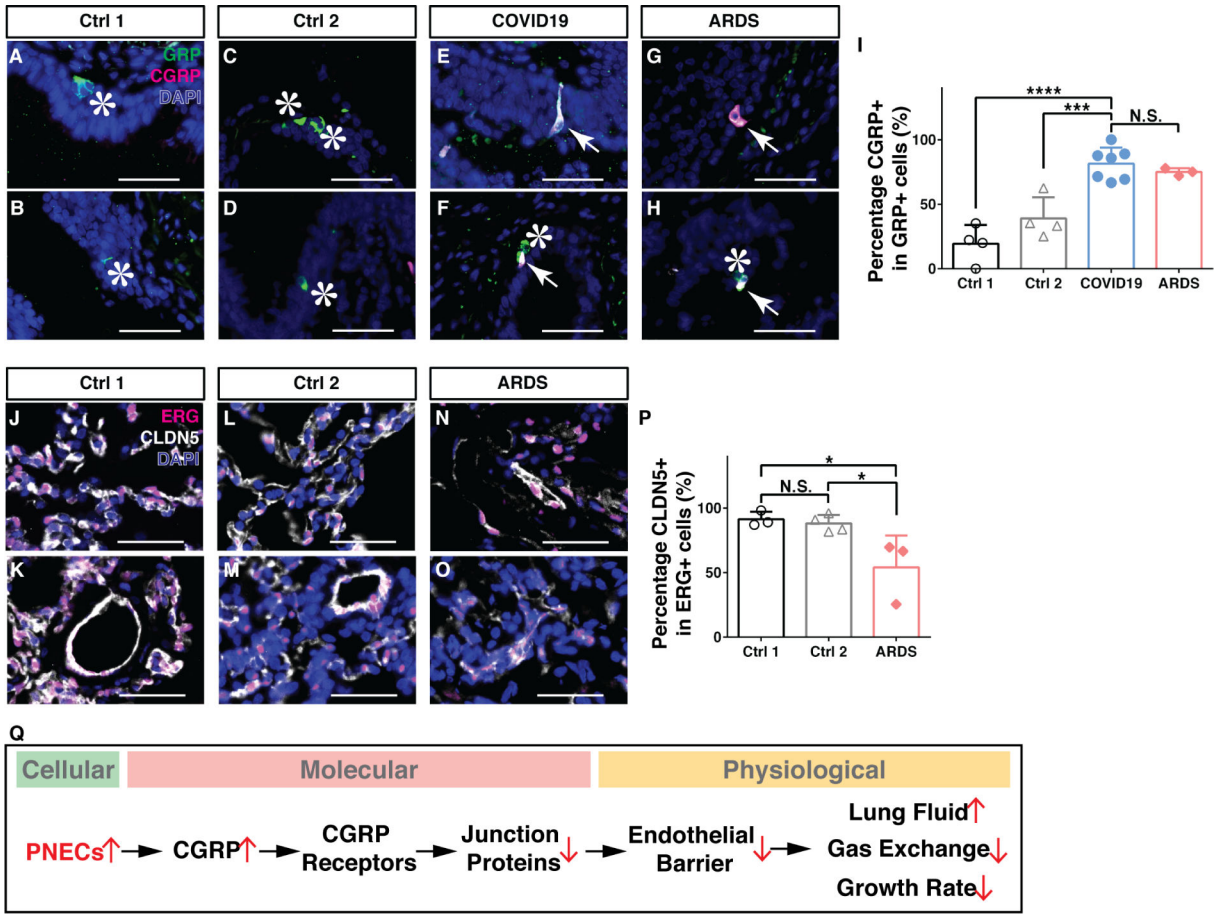

Figure 7. Human ARDS Lungs Exhibit Increased Proportion of CGRP+ PNECs and Reduced Tight Junction Protein Expression.

(A-H) Examples of anti-GRP staining (green, pan-PNEC marker) and anti-CGRP staining (magenta) showed differential proportion of CGRP+ PNECs in different groups of donor lungs. Ctrl 1: controls from lobectomy tissues without notable lung pathology (A, B), Ctrl 2: controls from autopsy tissues without notable lung pathology (C, D), COVID-19 ARDS samples (E, F), and non-COVID-19 ARDS samples (G, H). Asterisks indicate CGRP-negative PNECs; arrows indicate CGRP-positive PNECs.

(I) Percentages of CGRP+ PNECs in all GRP+ PNECs in noted sample groups. Each dot represents averaged data from one donor across multiple sections.

(J-O) Representative images of anti-ERG staining (magenta, endothelial marker) and anti-CLDN5 staining (white) showed decrease of CLDN5 level in non-COVID-19 ARDS samples. Ctrl 1 (J, K), Ctrl 2 (L, M) and ARDS (N, O) groups are the same as described in A-H.

(P) Percentages of CLDN5+ cells in ERG+ endothelial cells in noted sample groups. Each dot represents averaged data from one donor across multiple sections. (Q) A model for PNEC function in the control of lung fluid balance. In NEHI, PNEC hyperplasia led to increased neuropeptides such as CGRP, which signal to pulmonary endothelial cells to disrupt barrier integrity, leading to excess extravascular lung fluid as well as gas exchange deficiency. One-way ANOVA Tukey's multiple comparisons test was used for P and I. N.S.

not significant, p≥0.05. * for p<0.05, ** for p<0.01, *** for p<0.001, **** for p<0.0001. Error bars represent means ± SD.
See also Table S2.

KEY RESOURCES TABLE

REAGENT or RESOURCE	SOURCE	IDENTIFIER
Antibodies		
Mouse monoclonal anti-beta-actin	Novus	Cat# NB600-501; RRID: AB_10077656
Rat monoclonal anti-CDH5	BD Biosciences	Cat# 562795; RRID: AB_2737800
Rabbit polyclonal anti-Calcitonin Gene Related Peptide (CGRP)	Sigma-Aldrich	Cat# C8198; RRID: AB_259091
Mouse monoclonal anti-CLDN5	Thermo Fisher Scientific	Cat# 35-2500, RRID: AB_2533200
Mouse monoclonal anti-FOXJ1	Thermo Fisher Scientific	Cat# 14-9965-80; RRID: AB_1548836
Mouse monoclonal anti-HOPX	Santa Cruz	Cat# sc-398703; RRID: AB_2687966
Mouse monoclonal anti- MUC5AC	Sigma-Aldrich	Cat# 929M-9
Rabbit polyclonal anti-NKX2-1 (TTF1)	Seven Hills Bioreagents	Cat# WRAB-1231; RRID: AB_2832953
Rabbit polyclonal anti-SCGB1A1	Seven Hills Bioreagents	Cat # WRAB-3950
Rabbit polyclonal anti-pro-SPC	Sigma-Aldrich	Cat# AB3786
Mouse monoclonal anti-SOX2	Santa Cruz	Cat# sc-365823; RRID: AB_10842165
Rabbit polyclonal anti-Synaptophysin (SYP)	Fisher Scientific	Cat# RB-1461-P1; RRID: AB_60083
Rabbit polyclonal anti-bombesin	ImmunoStar	Cat# 20073; RRID: AB_572221
Mouse monoclonal anti-human CD31	Agilent	Cat# GA610; RRID: AB_2892053
Mouse monoclonal anti-human CD31	Agilent	Cat# GA610; RRID: AB_2892053
Rabbit monoclonal anti-human CLDN-5	Thermo Fisher Scientific	Cat# MA5-32614; RRID: AB_2809891
Rabbit monoclonal anti-ERG	Abcam	Cat# ab92513, RRID: AB_2630401
Goat polyclonal anti-Human PROX1	R&D Systems	Cat# AF2727; RRID: AB_2170716
PE anti-mouse CD31 (PECAM-1) antibody	BioLegend	Cat# 160203; RRID: AB_2860750
Brilliant Violet 510 (TM) anti-mouse CD45 antibody	BioLegend	Cat# 103137; RRID: AB_2561392
APC anti-mouse CD326 (Ep-CAM) antibody	BioLegend	Cat# 118214; RRID: AB_1134102
Rat Anti-CD16 / CD32 Monoclonal Antibody, Unconjugated	BD Biosciences	Cat# 553141; RRID: AB_394656
Goat anti-mouse FITC	Jackson Immunoresearch Labs	Cat# 115-095-166, RRID: AB_2338601
Goat anti-rabbit FITC	Thermo Fisher Scientific	Cat# A-11008; RRID: AB_143165
Donkey anti-rat AF488	Jackson Immunoresearch Labs	Cat# 712-545-150; RRID: AB_2340683
Goat anti-mouse Cy3	Jackson Immunoresearch Labs	Cat# 115-165-003; RRID: AB_2338680
Goat anti-rabbit Cy3	Jackson Immunoresearch Labs	Cat# 111-165-003; RRID: AB_2338000
Goat anti-mouse Cy5	Jackson Immunoresearch Labs	Cat# 115-175-166; RRID: AB_2338714
Donkey anti-mouse IRDye 680RD	LI-COR	Cat# 925-69072
Goat anti-rat IRDye 680LT	LI-COR	Cat# 925-68029

REAGENT or RESOURCE	SOURCE	IDENTIFIER
Critical commercial assays		
Chromium single cell RNA sequencing chemistry kit v3	10X Genomics	N/A
Chemicals, peptides, and recombinant proteins		
Tamoxifen	Sigma-Aldrich	T5648, CAS 10540-29-1
Click-iT™ EdU Cell Proliferation Kit	Thermo Fisher Scientific	Cat# C10337
CGRP (Rat) EIA Kit	Cayman Chemicals	Cat# 589001
DMSO	Sigma-Aldrich	Cat# D2650
Synthesized CGRP	Sigma-Aldrich	Cat# C0292
BIBN-4096	Fisher Scientific	Cat# 45-611-0
Bicuculline	Fisher Scientific	Cat# 01-305-0
MICROFIL® Silicone Rubber Injection Compounds	Flow-Tech Inc.	Cat# MV122
Methyl Salicylate	Sigma-Aldrich	Cat# M6752
DAPI	Sigma-Aldrich	Cat# D9542
Deposited data		
P22 Ctrl mice and NEHI mutants endothelial and epithelial cells single-cell RNA-seq data	This paper	GEO: GSE171907
P22 Ctrl mice, NEHI mutants and BIBN-treated NEHI mutants western blot raw data	This paper	Mendeley database DOI:10.17632/yk3hztpt49.1
Experimental models: Organisms/strains		
Mouse: Ai14, B6.Cg-*Gt(ROSA)26Sor*$^{tm14(CAG-tdTomato)Hze}$/J	The Jackson Laboratory	JAX: 007914
Mouse: *Ascl1*^{creER}, *Ascl1*$^{tm1.1(Cre/ERT2)Jejo}$/J	The Jackson Laboratory	JAX: 012882
Mouse: *Ascl1*^{Fl}, Ascl1^{tm2Fgu}	Guoli Dai, Francois Guillemot	(Pacary et al., 2011)
Mouse: *Calca*$^{-}$, B6.129P2(Cg)-*Calca*$^{tm1.1(EGFP/HBEGF)Mjz}$/Mmnc	MMRRC	RRID: MMRRC_036773-UNC
Mouse: *Crlr*^{Fl}, Calcrl^{tm1Kmca}	Kathleen Caron	(Fritz-Six et al., 2008)
Mouse: *Cdh5-cre*, B6;129-Tg(Cdh5-cre)1Spe/J	The Jackson Laboratory	JAX: 017968
Mouse: *Tac1*$^{-}$, B6.Cg-*Tac1*^{tm1Bbm}/J	The Jackson Laboratory	JAX: 004103
Mouse: *Nkx2-1*^{creER}, *Nkx2-1*$^{tm1.1(cre/ERT2)Zjh}$/J	The Jackson Laboratory	JAX: 014552
Mouse: *Nkx2-1*^{R161L}	This paper	N/A
Mouse: *Nkx2-1*^{Fl}, Nkx2-1^{tm2Shk}	Shioko Kimura	(Kusakabe et al., 2006)
Mouse: *Shh*^{cre}, B6.129S6-$^{Shhtm2(cre/ERT2)Cjt}$/J	Cliff Tabin	JAX: 005623
Oligonucleotides		
qPCR Primer: *Actb* Forward: CGGCCAGGTCATCACTATTGGCAAC	This paper	N/A
qPCR Primer: *Actb* Reverse: GCCACAGGATTCCATACCCAAGAAG	This paper	N/A
qPCR Primer: *Ascl1* Forward: TCTGGCAAGATGGAGAGTGGAGC	This paper	N/A
qPCR Primer: *Ascl1* Reverse: AAAGAAGCAGGCTGCGGGAG	This paper	N/A
qPCR Primer: *Atf2* Forward: GAGGAGCCTTCTGTTGTAGAAAC	This paper	N/A
qPCR Primer: *Atf2* Reverse: GACGAACGATAGCTGATGTGG	This paper	N/A

REAGENT or RESOURCE	SOURCE	IDENTIFIER
qPCR Primer: *Calca* Forward: CCTTTCCTGGTTGTCAGCATCTTG	This paper	N/A
qPCR Primer: *Calca* Reverse: CTGGGCTGCTTTCCAAGATTGAC	This paper	N/A
qPCR Primer: *Cldn5* Forward: ACGGGAGGAGCGCTTTAC	This paper	N/A
qPCR Primer: *Cldn5* Reverse: GTTGGCGAACCAGCAGAG	This paper	N/A
A complete list of qPCR primers can be found in Table S3.		
Software and algorithms		
ImageJ	(Schneider et al., 2012)	https://imagej.nih.gov/ij/
Prism 6	Graph Pad Software	https://www.graphpad.com/scientificsoftware/prism/
Seurat V3	Satija Lab	https://satijalab.org/seurat/
CellChat	(Jin et al., 2021)	https://github.com/sqjin/CellChat